

Boson Sampling as a Probe of Chaotic and Integrable Quantum Dynamics

Yuancheng Zhan^{1,2}, Khen Cohen^{3†}, Norman T.W. Koo^{2†}, Kian Hwee Lim^{2,4†},
Hui Zhang^{1,5}, Lingxiao Wan¹, Sanghoon Chae¹, Ai Qun Liu⁶,
Victor M Bastidas⁷, Yaron Oz^{3*}, Leong-Chuan Kwek^{1,2,8*}

¹School of Electrical and Electronic Engineering (EEE), Nanyang Technological University, 50 Nanyang Ave, Singapore, 639798, Singapore.

²Centre for Quantum Technologies (CQT), National University of Singapore, 3 Science Drive 2, Singapore, 117543, Singapore.

³The School of Physics and Astronomy, Tel-Aviv University, Haim Levanon, Tel Aviv, 69978, Israel.

⁴MajuLab, CNRS-UCA-SU-NUS-NTU International Joint Research Laboratory, 3 Science Drive 2, 117543, Singapore.

⁵School of Physics Science and Engineering, Tongji University, Yangpu District, Shanghai, 200092, China.

⁶Institute of Quantum Technologies, The Hong Kong Polytechnic University, 11 Yuk Choi Road, Hong Kong, 999077, China.

⁷NTT Basic Research Laboratories & Research Center for Theoretical Quantum Physics, Morinosato-Wakamiya, Kanagawa, 2430198, Japan.

⁸National Institute of Education, Nanyang Technological University, 1 Nanyang Walk, Singapore, 637616, Singapore.

*Corresponding authors' e-mails: yaronoz@tauex.tau.ac.il; cqtklc@gmail.com;

†These authors contributed equally to this work.

Abstract

Quantum technologies have become a powerful paradigm for quantum information and simulation, while quantum chaos plays a key role in understanding complex quantum dynamics. Integrated photonics offers unique advantages for quantum applications, including high-speed operation, scalability, and programmable unitary transformations. However, probing quantum chaos on integrated photonic platforms remains largely unexplored because a clear connection between programmable photonic dynamics and established chaos diagnostics is still lacking. In this work, we establish Fock-state boson sampling as a practical probe of quantum chaos by exploiting the sensitivity of multiphoton interference to the random-matrix properties of underlying single-particle unitary dynamics. More importantly, we design and fabricate a programmable silicon quantum photonic chip to experimentally implement this framework, achieving the first integrated-photonics demonstration of quantum-chaos probes based on boson sampling. Experimental results show that the three complementary probes proposed in this work, namely the distance to Porter–Thomas statistics, Shannon entropy, and Out-of-Time-Ordered-Correlator-equivalent observables, exhibit close agreement with theoretical predictions and consistently distinguish chaotic and integrable dynamics. Our work provides a scalable route for investigating complex quantum dynamics on programmable photonic platforms while leveraging the intrinsic advantages of boson sampling through multiphoton interference and complex output statistics.

Keywords: Quantum Chaos, Integrated Photonic Chip, Boson Sampling, Quantum Photonics

1 Introduction

Quantum technologies have emerged as a central paradigm in modern science, underpinning advances in quantum information processing [1–3], cryptography [4–6], and quantum simulation [7, 8]. Among the various physical platforms, photonic architectures offer distinct advantages for quantum applications [4, 9–13], including low decoherence, high-speed information processing, and the ability to implement large-scale, programmable unitary transformations via integrated optical networks [14–17]. These properties make integrated photonic systems an attractive platform for scalable quantum computing protocols and for experimentally studying fundamental aspects of quantum mechanics. Quantum chaos plays an important role in understanding thermalization, ergodicity, information spreading, and the emergence of complex dynamics in quantum systems [18]. To characterize such behavior, quantum chaos is typically identified through spectral statistics, such as the spectral form factor (SFF) [19], or dynamically via the Out-of-Time-Ordered Correlator (OTOC) [20, 21]. These signatures have been extensively investigated in trapped ions [22], superconducting circuits [23], and nuclear magnetic resonance [24]. However, existing studies of quantum chaos often rely on specific dynamical models with direct semiclassical limits, such as atom–field interaction systems and related chaos models [25–27], making their implementation inherently model-dependent. Moreover, in quantum optical systems, previous investigations have mainly focused on free-space implementations [26–28]. Programmable integrated photonic platforms remain largely unexplored so far because a clear connection between programmable photonic dynamics and established probes of quantum chaos is still lacking. As a result, the advantages of integrated photonics have not yet been fully exploited in this area.

Boson sampling is a quantum computational model based on multiphoton interference in linear-optical networks [29–32], where output probabilities are determined by matrix permanents and are believed to be classically intractable to simulate for sufficiently large systems. Boson sampling has been extensively explored as a promising route toward quantum computational advantages in photonic systems, such as applications in molecular spectra [16, 33], graph theory [33, 34], and quantum machine learning [35, 36]. More importantly, the complexity of boson sampling output statistics suggests a potential connection to quantum chaos, where signatures of the underlying dynamics may be reflected in the measured probability distributions.

Building upon this potential connection, our first contribution is to establish Fock-state boson sampling as a practical probe of quantum chaos. We show that the temporal evolution of boson sampling output statistics generated from the time evolution of an underlying Hamiltonian can reveal signatures of the system dynamics and therefore be used to distinguish chaotic and integrable behavior. This arises because the bosonic interference of indistinguishable photons makes the time evolution of the resulting output probability distribution sensitive to the random-matrix properties of the underlying single-particle unitary evolution, enabling signatures of chaotic dynamics to be extracted from the measured statistics. Based on this principle, we identify three complementary diagnostic probes from the temporal behavior of the boson sampling output distributions. First, we find that the distribution of output probability values approaches Porter–Thomas (PT) statistics [37] for chaotic dynamics at some predictable value of time, providing a statistical signature of the regime in which the underlying unitary evolution becomes closer to Haar-random behavior [19]. Second, we show that the temporal evolution of the Shannon entropy [38, 39] distinguishes the two regimes, where chaotic dynamics produce more delocalized output distributions and correspondingly larger entropy values than integrable dynamics. Third, we extract OTOC-equivalent observables from output probabilities based on the mapping between boson sampling statistics and four-point OTOCs established in our previous work [40]. We find that chaotic dynamics exhibit stronger delocalization in Hilbert space and broader frequency content in their temporal evolution than integrable dynamics.

To implement these ideas experimentally, our second contribution is the realization of these quantum-chaos probes using Fock-state boson sampling on an integrated photonic platform, allowing the entire probing process to benefit from the scalability, reconfigurability, and quantum advantages of photonic chips. We employ a random-matrix framework in which a single parameter continuously tunes the crossover between integrable and chaotic regimes, providing a compact and naturally programmable implementation on photonic hardware. Experimentally, we design and implement a silicon integrated photonic chip supporting programmable M -mode unitary transformations with N input

photons. In our demonstration, an eight-mode photonic processor with two indistinguishable photons realizes integrable and chaotic random-matrix dynamics through arbitrary unitary programming and multiphoton correlation measurements using superconducting nanowire single-photon detectors. Experimental results show that the proposed probes consistently distinguish integrable (Poissonian) and chaotic (Gaussian Orthogonal Ensemble, GOE) dynamics with high accuracy and efficiency while providing, to the best of our knowledge, the first experimental realization of boson sampling-based quantum-chaos probes.

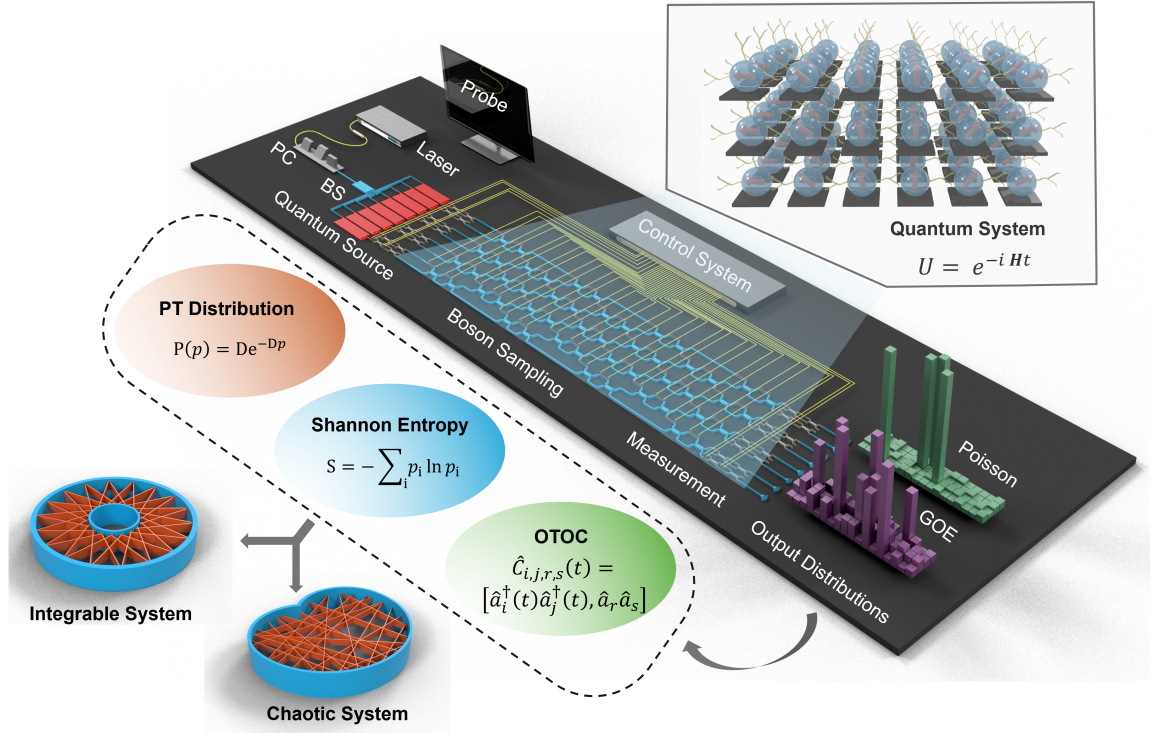


Fig. 1 Workflow for distinguishing chaotic and integrable dynamics using on-chip boson sampling. A quantum system undergoing unitary evolution $U = e^{-iHt}$ is mapped onto an integrated photonic platform, where Fock-state boson sampling is implemented using a pump laser, polarization controller (PC), beam splitter (BS), and spiral waveguides for photon-pair generation, followed by a programmable optical network and correlation measurements. The measured output probability distributions are then used to extract three quantitative indicators: the Wasserstein distance between the empirical distribution and the PT distribution, the Shannon entropy of the output distribution, and OTOC-equivalent observables derived from the output probabilities. Together, these metrics provide a comprehensive framework for distinguishing chaotic and integrable quantum dynamics.

Figure 1 summarizes the overall workflow of this work. A quantum system undergoing unitary evolution $U = e^{-iHt}$ is mapped onto a programmable integrated photonic platform, where Fock-state boson sampling is implemented through photon-pair generation, programmable optical transformations, and multiphoton correlation measurements. The time evolution of the resulting output probability distributions encodes information about the underlying dynamics and serves as experimentally accessible observables for probing quantum chaos. The measured statistics are subsequently analyzed using three complementary probes: PT statistics, Shannon entropy, and OTOC-equivalent observables, providing a unified framework for distinguishing integrable and chaotic dynamics on programmable integrated photonic hardware.

2 Theory

2.1 Boson Sampling

To probe quantum dynamics using boson sampling, we consider an N -photon input state propagating through an M -mode interferometer. Programmable unitaries $U^{(l)}(t_k) \in U(M)$ generated by the Hamiltonian ensembles are implemented on an integrated photonic chip, where l labels the Hamiltonian realization and t_k denotes the k -th sampled evolution time. The corresponding unitary evolution is given by $U(t) = e^{-iHt}$ in the optical-mode basis, where each mode corresponds to a basis state $|j\rangle = \hat{a}_j^\dagger |0\rangle = |0_1, 0_2, \dots, 1_j, \dots, 0_M\rangle$ and \hat{a}_j^\dagger denotes the creation operator of mode j . Bosonic interference between indistinguishable photons makes the measured output statistics highly sensitive to the underlying unitary dynamics and their associated random-matrix properties.

Based on this mapping, an N -photon input Fock state $|\mathbf{n}^{\text{in}}\rangle = |n_1^{\text{in}}, \dots, n_M^{\text{in}}\rangle$ evolves through the interferometer according to $\hat{a}_i^\dagger(t_k) = \sum_{j=1}^M U_{ij}^{(l)}(t_k) \hat{a}_j^\dagger$. The probability of observing an output occupation pattern $\mathbf{n}^{\text{out}} = (n_1^{\text{out}}, \dots, n_M^{\text{out}})$ is then given by

$$p_{\mathbf{n}^{\text{out}}}^{(l)}(t_k) = \frac{\left| \text{Per} \left[U_{\mathbf{n}^{\text{out}}, \mathbf{n}^{\text{in}}}^{(l)}(t_k) \right] \right|^2}{\prod_i n_i^{\text{out}}! \prod_j n_j^{\text{in}}!}, \quad (1)$$

where $U_{\mathbf{n}^{\text{out}}, \mathbf{n}^{\text{in}}}^{(l)}(t_k)$ is the $N \times N$ submatrix constructed by repeating rows according to the output occupations \mathbf{n}^{out} and columns according to the input occupations \mathbf{n}^{in} . For convenience, we collect all output probabilities $p_{\mathbf{n}^{\text{out}}}^{(l)}(t_k)$ into the probability vector and write it as $\mathbf{p}(t)$ when realization and time indices are not essential. The permanent structure (Per) makes output probabilities a highly nontrivial function of the underlying unitary evolution. We retain only two-click collision-free events and construct conditional probability distributions over collision-free output configurations. This approach avoids the need for photon-number-resolving detection while preserving the relevant statistical properties of the output distributions. As shown in Appendix A, this restriction preserves the relevant statistical properties of the conditional probability distributions used throughout this work, provided that the collision-free fraction D/N_0 remains sufficiently close to unity, where $D = \binom{M}{N}$ and $N_0 = \binom{M+N-1}{N}$ denote the number of collision-free and total output configurations, respectively. This condition is satisfied in our experiment with $D/N_0 \simeq 0.78$ (see Eq. S2 and Eq. S3).

2.2 Random-Matrix Hamiltonians for Integrable and Chaotic Dynamics

To generate integrable and chaotic dynamics, we employ a random-matrix Hamiltonian family [41, 42],

$$H = \frac{H_0 + \lambda V}{\sqrt{1 + \lambda^2}}, \quad (2)$$

where H_0 is a diagonal matrix with independent Gaussian entries, $(H_0)_{ii} \sim \mathcal{N}(0, 1)$ and V is a $d \times d$ real symmetric matrix drawn from the GOE ensemble, with variances $2/d$ and $1/d$ for diagonal and off-diagonal elements, respectively. Here d denotes the Hilbert-space dimension, which equals the number of optical modes in the experimental implementation ($d = M$). H_0 describes an integrable system with uncorrelated energy levels, whereas the GOE perturbation V introduces level mixing and repulsion, driving the system toward chaotic behavior. The perturbation strength λ is commonly expressed through the dimensionless parameter $\Lambda = \lambda^2 d / 2\pi$, which characterizes the relative strength of the integrability-breaking perturbation with respect to the mean level spacing. For $\Lambda \ll 1$, level mixing is weak and the system exhibits integrable (Poissonian) statistics, whereas for $\Lambda \gg 1$, strong mixing leads to chaotic (GOE) behavior. Accordingly, varying Λ drives a continuous crossover from Poissonian to GOE statistics. In this work, we focus on the two limiting cases, while intermediate regimes remain experimentally accessible.

We sample ensembles $\{H_0^{(l)}\}$ and $\{V^{(l)}\}$ and consider two representative values, $\Lambda = 0.01$ and $\Lambda = 1000$, corresponding to integrable ($\{H^{(l)}\}_{\text{nc}}$) and chaotic ($\{H^{(l)}\}_{\text{c}}$) regimes, respectively. For each realization, the Hamiltonians are evolved to five discrete time points $t_k \in [t_1, \dots, t_5]$, generating two sets of unitary matrices, $\{U^{(l)}(t_k) = e^{-iH^{(l)}t_k}\}_{\text{nc}}$ and $\{U^{(l)}(t_k) = e^{-iH^{(l)}t_k}\}_{\text{c}}$ (see Appendix B

for detailed settings). These unitary matrices are then programmed onto the photonic chip, where boson sampling is performed using a fixed input state to obtain the corresponding output probability distributions $\{\mathbf{p}^{(l)}(t_k)\}_{\text{nc}}$ and $\{\mathbf{p}^{(l)}(t_k)\}_{\text{c}}$. For each evolution time, the probe quantities are computed from the realization-dependent output distributions and subsequently averaged over the corresponding ensembles. The three probes and the corresponding experimental results are defined and discussed in Section 4. Although the implemented dynamics are generated through single-particle unitary evolution, bosonic indistinguishability produces nontrivial multiphoton interference at the output, allowing signatures of the underlying random-matrix dynamics to emerge in the measured probability distributions. Our experimental implementation employs the random-matrix Hamiltonian family H_Λ because of its theoretical simplicity and controllability. More generally, the proposed framework can be naturally extended to more general many-body spin Hamiltonians (see Appendix C for further details).

3 Experimental Implementation

In the experiment, we designed and fabricated an integrated photonic chip capable of integrating photon generation, manipulation, and measurement within a compact and reconfigurable architecture. The overall experimental setup is shown in Fig. 2a, following a comprehensive characterization of the integrated photonic system (the detailed experimental procedure is described in Appendix D.1). Figure 2b illustrates our experimental quantum photonic circuit. The 8-mode integrated chip, measuring $10 \text{ mm} \times 1.6 \text{ mm}$, provides a compact architecture with 100 independently adjustable phase shifters. Details of the calibration of these adjustable phases are discussed in Appendix D.2. Each phase shifter is controlled externally via digital-to-analog converters (DACs), with connections made through two rows of metal pads bonded by gold wires on the upper and lower sides of the printed circuit board. This architecture is compatible with larger programmable photonic systems and therefore provides a pathway toward scaling to higher-dimensional implementations.

Photon pairs are generated through spontaneous four-wave mixing (SFWM) in eight spiral-waveguide quantum sources, as shown in Fig. 2c. To excite these sources simultaneously, the pump light is distributed into eight channels through a 1-to-8 beam splitter network (Fig. 2d), forming an effective eight-input configuration. The photon sources exhibit high interference visibility, with detailed characterization and error analysis provided in Appendices D.3 and D.4, respectively. By tuning the pump power using MZIs placed before the quantum source, each source achieves a controllable photon generation rate of approximately 500 kHz. Following generation, residual pump photons at wavelengths around 1545 nm and 1555 nm are filtered using the Asymmetric Mach-Zehnder interferometer (AMZI), as illustrated in Fig. 2e. This filtering stage suppresses unwanted pump light that could otherwise degrade interference in the subsequent optical circuit. The filtered photons are then injected into a reconfigurable optical network capable of implementing arbitrary unitary transformations via the Clements decomposition protocol [43]. This approach decomposes any unitary matrix into a sequence of tunable MZIs (Fig. 2f), achieving an average unitary fidelity of 0.93 (see Appendix D.5 for details). This circuit forms the computational core of quantum chaos experiments, with high flexibility in parameter selection. Finally, photons exiting the circuit are coupled off-chip through a fiber grating array and detected using high-efficiency superconducting nanowire single-photon detectors. The total optical loss from chip to detector is approximately 10 dB, while the detector efficiency reaches $\sim 88\%$, with a dark count rate of about 50 s^{-1} . In data acquisition, only events where the number of detected photons matches the number of injected photons are retained for analysis (see Appendix A for details). Since our diagnostics rely on statistical properties of the output distribution rather than exact amplitudes, they are robust to moderate deviations from the ideal unitary, provided multiphoton indistinguishability and interference visibility remain high.

Boson sampling experimental results are shown in Figures 2g,h for the Poissonian and GOE cases, respectively, corresponding to the integrable and chaotic ensembles introduced in Section 2.2. For each evolution time point $t \in [1, 1.79, 29.29, 100, 1000]$, we show five randomly selected realizations, while detailed settings are provided in Appendix B. From the results, we observe that for all evolution times, the experimental measurements (red) are in good agreement with the theoretical predictions (blue), demonstrating the accuracy of the experimentally obtained output statistics. The sources of residual discrepancies include device imperfections and experimental noise contributions, detailed in Appendix D.4. In addition, clear differences between the Poissonian and GOE cases can

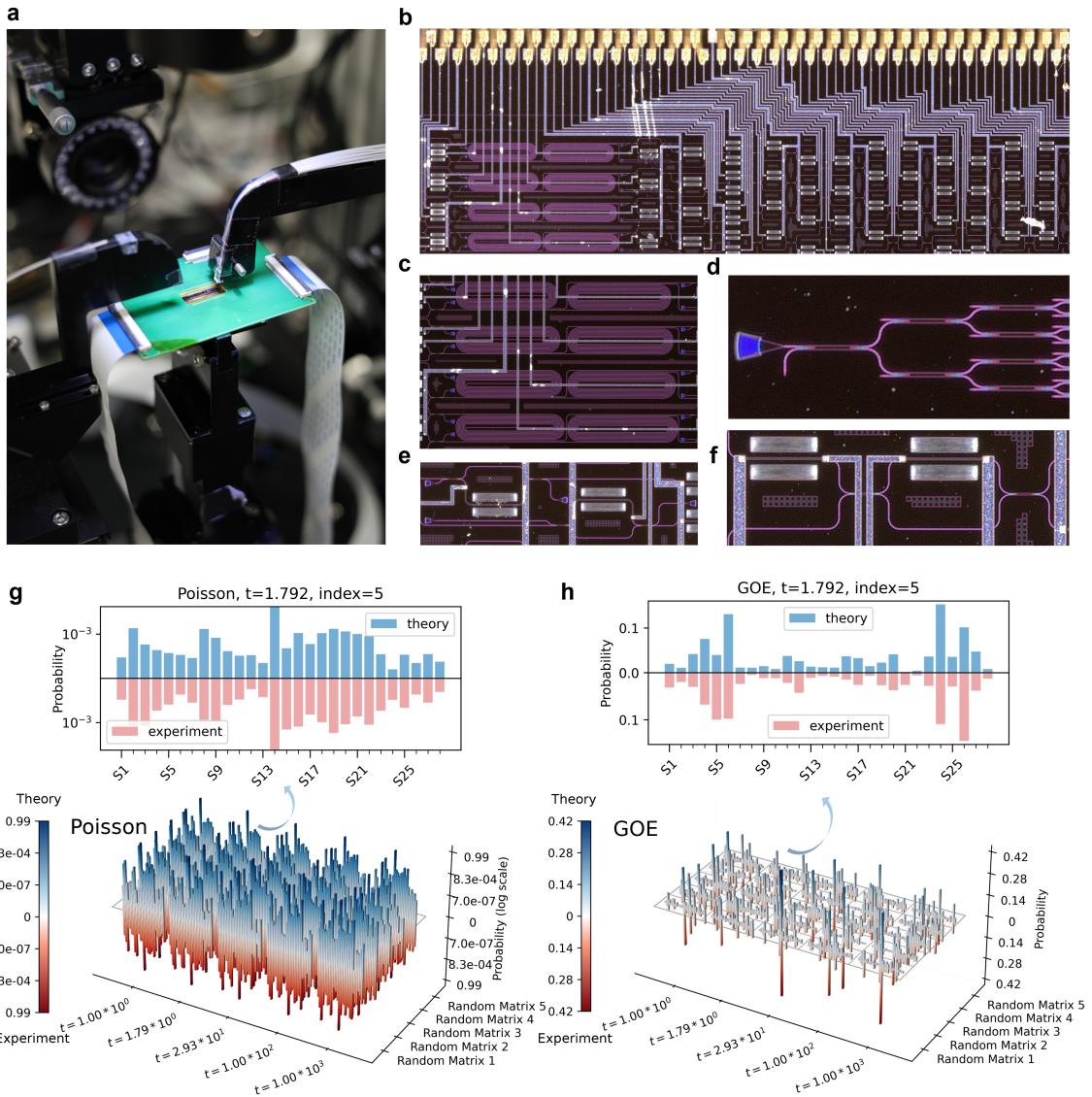


Fig. 2 Experimental implementation of the on-chip boson sampling platform. **a**, Schematic overview of the experimental setup integrating photon generation, manipulation, and measurement on a single photonic chip. **b**, The 8-mode reconfigurable photonic circuit. **c**, Spiral waveguide structures used for photon-pair generation via SFWM. **d**, 1-to-8 beam splitter network for distributing input light. **e**, AMZI is used for pump filtering. **f**, MZI structure. **g**, Integrable dynamics. Top: Enlarged view of the output probability distribution at $t = 1.792$, where blue and red bars denote the theoretical and experimental results, respectively. The full distribution consists of 28 two-photon basis states, labeled as s_1, \dots, s_{28} , e.g., $s_1 = |1_1, 1_2, 0_3, \dots, 0_8\rangle$, $s_2 = |1_1, 0_2, 1_3, \dots, 0_8\rangle$, ..., $s_{28} = |0_1, \dots, 0_6, 1_7, 1_8\rangle$. Bottom: Experimental and theoretical output distributions for five randomly selected realizations at evolution times $t \in [1, 1.79, 29.29, 100, 1000]$. **h**, Chaotic dynamics. Same as in **g**, but for the GOE Hamiltonian ensemble.

already be observed from the measured output distributions. In the Poissonian regime, only a few output configurations carry significant probability weight, while most remain close to zero, indicating a more localized distribution. In contrast, the GOE case exhibits probability spreading over more output configurations, reflecting stronger delocalization expected for chaotic dynamics. This qualitative distinction provides an intuitive picture for the quantitative diagnostic analysis presented in Section 4.

4 Results

Using the experimentally measured boson sampling distributions $\{\mathbf{p}^{(l)}(t)\}$ introduced above, we now analyze how signatures of quantum chaos emerge in the output statistics. Our objective is to distinguish integrable and chaotic dynamics through ensemble-averaged properties of the measured distributions. To this end, we employ three complementary probes: the proximity to PT statistics, the Shannon entropy, and OTOC-equivalent observables derived from output probabilities. Together, these quantities provide a unified characterization of the statistical, dynamical, and delocalization properties associated with quantum chaos.

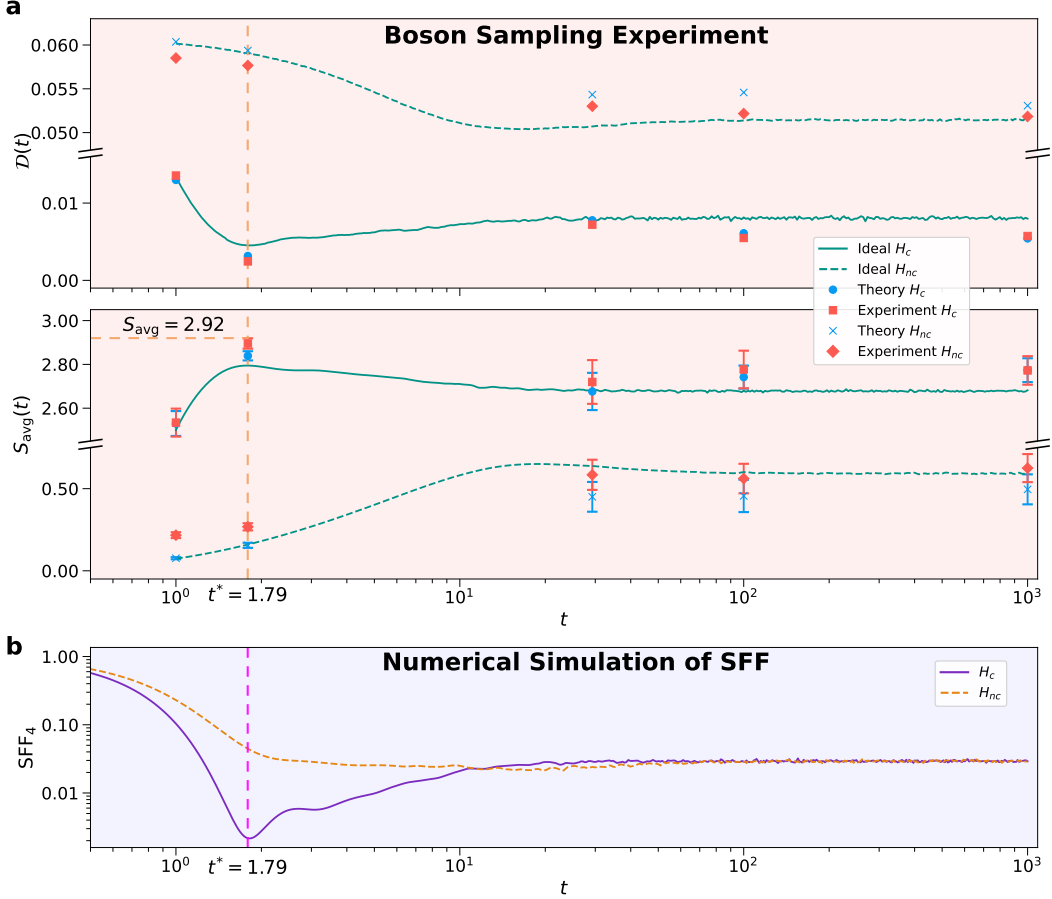


Fig. 3 Experimental results for the first two probes of chaos that are extractable from $\mathbf{p}(t)$, as well as the numerically simulated 4-point SFF for both H_C and H_{nc} . **a**, In the top panel, for both H_C and H_{nc} respectively, we study $\mathcal{D}(t)$ as defined in Eq. 4. In the bottom panel, for H_C and H_{nc} respectively, we study $S_{avg}(t_k)$ as defined in Eq. 6. In these plots, we show the experimental results (red points) obtained by performing boson sampling on the unitaries on the photonic chip (see Appendix B for more details). The corresponding theoretical results assuming an ideal Boson Sampling on the same unitaries (blue points) are also plotted. In the bottom panel, the error bars are the standard error in the mean value of the probe due to the finite number of instances used for Eq. 2. We note the close agreement between the theoretical results and the experimental results. The ideal curves in green describe the case where we have a large number of instances (2000) for many time points. The difference between the theoretical and the ideal result is due to the small number of samples per time point in the theoretical case. **b**, As expected, we see a dip-ramp-plateau structure in H_C . The minimum of the SFF for H_C is at $t^* = 1.79$. We note that for H_C , the minimum of the SFF corresponds with the dip in $\mathcal{D}(t)$ and the peak in $S_{avg}(t)$, as expected.

4.1 Distance from Porter–Thomas Distribution

For each evolution time t , the boson sampling experiment produces a set of output probability distributions $\{\mathbf{p}^{(l)}(t)\}$ over different Hamiltonian realizations $l = 1, \dots, n_t$ (n_t is the number of realizations at time t). To characterize their statistical properties, we construct the empirical distribution

of probability values by pooling all collision-free output probabilities across realizations and output configurations,

$$f_t(p) = \frac{1}{N_{\text{tot}}} \sum_{l=1}^{n_t} \sum_{i=1}^D \delta(p - p_i^{(l)}(t)), \quad (3)$$

where $i = 1, \dots, D$ labels the allowed output configurations and $N_{\text{tot}} = n_t D$ denotes the total number of sampled probabilities. The distribution $f_t(p)$ therefore represents the empirical histogram of output probability values.

A key finding of our work is the connection between the spectral structure of quantum chaos and experimentally accessible boson sampling statistics. For chaotic Hamiltonians, the unitary evolution e^{-iHt} is expected to approach Haar-random behavior at intermediate times, corresponding to the minimum of the spectral form factor (detailed in Appendix E). Since boson sampling with Haar-random unitaries produces output probabilities following the Porter–Thomas distribution on average, the empirical probability distribution $f_t(p)$ is expected to approach $P_{\text{PT}}(p) = D e^{-Dp}$ in the large- D limit when the SFF reaches a minimum (with finite- D corrections discussed in Appendix A). This motivates using the distance between the measured distribution and the Porter–Thomas distribution as an experimentally accessible probe of chaos. To quantify this proximity, we compute the Wasserstein-1 distance [44] between the empirical distribution $f_t(p)$ and the Porter–Thomas distribution $P_{\text{PT}}(p)$

$$\mathcal{D}(t) = W_1(f_t(p), P_{\text{PT}}(p)) . \quad (4)$$

where W_1 is calculated from the corresponding cumulative distribution functions. The Wasserstein distance is particularly suitable because it directly measures the global discrepancy between two probability distributions and remains robust for finite-sample experimental data. Hence, for chaotic Hamiltonians, we expect that $\mathcal{D}(t)$ should exhibit a characteristic dip as a function of time, corresponding to the minimum of the spectral form factor, followed by a plateau at longer times. In contrast, for integrable dynamics no such feature is expected.

The experimental and theoretical results are shown in the top panel of Fig. 3a, together with ideal numerical curves obtained from larger ensembles and more densely sampled evolution times for comparison. For chaotic dynamics, $\mathcal{D}(t)$ exhibits a pronounced dip and approaches values close to zero around $t^* = 1.79$, which coincides with the minimum of the SFF shown in Fig. 3b. This agreement confirms the theoretical expectation that chaotic dynamics become increasingly similar to Haar-random behavior near the SFF dip region. Furthermore, we see a ramp and a plateau after the dip, corresponding to the SFF behavior as per Fig. 3b. In contrast, integrable dynamics consistently remain farther from the Porter–Thomas distribution throughout the evolution. Therefore, the proximity of the output statistics to Porter–Thomas behavior provides a direct experimental signature for distinguishing chaotic and integrable dynamics. Given the finite system size and limited number of time points in our experiment, we interpret the observed behavior of $\mathcal{D}(t)$ as a qualitative indicator rather than a precise reconstruction of the spectral form factor.

4.2 Shannon Entropy

The second complementary probe is the Shannon entropy of the output probability distribution. For each realization l and time t , the entropy of the corresponding probability vector $\mathbf{p}^{(l)}(t)$ is defined as

$$S^{(l)}(t) = - \sum_{i=1}^D p_i^{(l)}(t) \ln p_i^{(l)}(t), \quad (5)$$

where the summation runs over all collision-free output configurations. To characterize the ensemble behavior, we compute the average entropy over all n_{t_k} realizations at each evolution time t_k ,

$$S_{\text{avg}}(t_k) = - \frac{1}{n_{t_k}} \sum_{l=1}^{n_{t_k}} \sum_{i=1}^D p_i^{(l)}(t_k) \ln p_i^{(l)}(t_k). \quad (6)$$

which quantifies how uniformly the probability weight is distributed across the accessible output space. Lower entropy indicates that the probability distribution is concentrated on a small number

of configurations, whereas larger entropy corresponds to stronger delocalization over the accessible Hilbert space.

The central observation underlying this probe is that chaotic dynamics lead to stronger spreading of probability weight across the output space than integrable dynamics. Since chaotic evolution approaches Haar-random behavior near the dip region of the spectral form factor, the corresponding boson sampling distributions are expected to become maximally delocalized, resulting in a peak in the Shannon entropy. Detailed derivations are provided in Appendix E. For Haar-random unitaries, the expected entropy can be evaluated analytically as

$$\langle S \rangle_{\text{Haar}} = -1 + \sum_{i=1}^D \frac{1}{i}. \quad (7)$$

which gives the predicted maximum entropy

$$\max_t S_{\text{avg}}(t) \approx -1 + \sum_{i=1}^D \frac{1}{i} \approx 2.92 \quad (D = 28). \quad (8)$$

The experimental and theoretical results are shown in the bottom panel of Fig. 3a. For chaotic dynamics, $S_{\text{avg}}(t)$ exhibits a pronounced peak around $t^* = 1.79$, where the experimentally observed value approaches the predicted Haar limit of 2.92. This behavior is consistent with the expectation that chaotic evolution produces increasingly delocalized output distributions near the SFF dip region. In contrast, the entropy of integrable dynamics remains consistently lower throughout the evolution, indicating that the probability weight remains concentrated on a smaller subset of output configurations. Residual discrepancies between the experimental results and the predicted Haar limit mainly arise from finite-size effects and experimental limitations. Numerical simulations in Appendix F show that these finite-size effects decrease with increasing system size, leading to improved agreement with the Haar prediction and a clearer separation between chaotic and integrable dynamics. Additional deviations originate from experimental imperfections, including finite sampling statistics and hardware nonidealities, which are analyzed in Appendix E.4.

Therefore, the Shannon entropy of the boson sampling output distribution provides a second experimental signature for distinguishing chaotic and integrable dynamics. Physically, this probe quantifies the degree of probability spreading in the accessible Hilbert space and provides a direct measure of the delocalization induced by chaotic dynamics.

4.3 OTOC-equivalent Observables

The third complementary probe of quantum chaos is constructed from OTOC-equivalent observables derived from boson sampling statistics. Instead of directly measuring conventional OTOCs, we exploit a mapping between boson sampling output probabilities and four-point correlators to obtain experimentally accessible signatures of information spreading and delocalization. This approach enables the dynamics of quantum chaos to be probed directly from measured output probabilities on a programmable photonic platform. To establish this connection, we use the mapping derived in our previous work [40], where the output probabilities of boson sampling with a two-photon Fock input are shown to be equivalent to four-point OTOCs of single-particle creation and annihilation operators. In particular, for a two-photon input state $\hat{a}_i^\dagger \hat{a}_j^\dagger |0\rangle$, the probability of detecting photons in output modes r and s can be expressed as

$$C_{i,j,r,s}^{(4)}(t) = \langle 0 | \hat{C}_{i,j,r,s}^\dagger(t) \hat{C}_{i,j,r,s}(t) | 0 \rangle, \quad (9)$$

where $\hat{C}_{i,j,r,s}(t) = [\hat{a}_i^\dagger(t) \hat{a}_j^\dagger(t), \hat{a}_r \hat{a}_s]$ and $\hat{a}_i^\dagger(t) = \sum_j U_{ij}(t) \hat{a}_j^\dagger$ is the time-evolved creation operator in the Heisenberg picture. These configuration-resolved output probabilities therefore act as OTOC-equivalent observables that probe the delocalization of single-particle excitations across optical modes through bosonic interference. Since the implemented dynamics originate from single-particle unitary

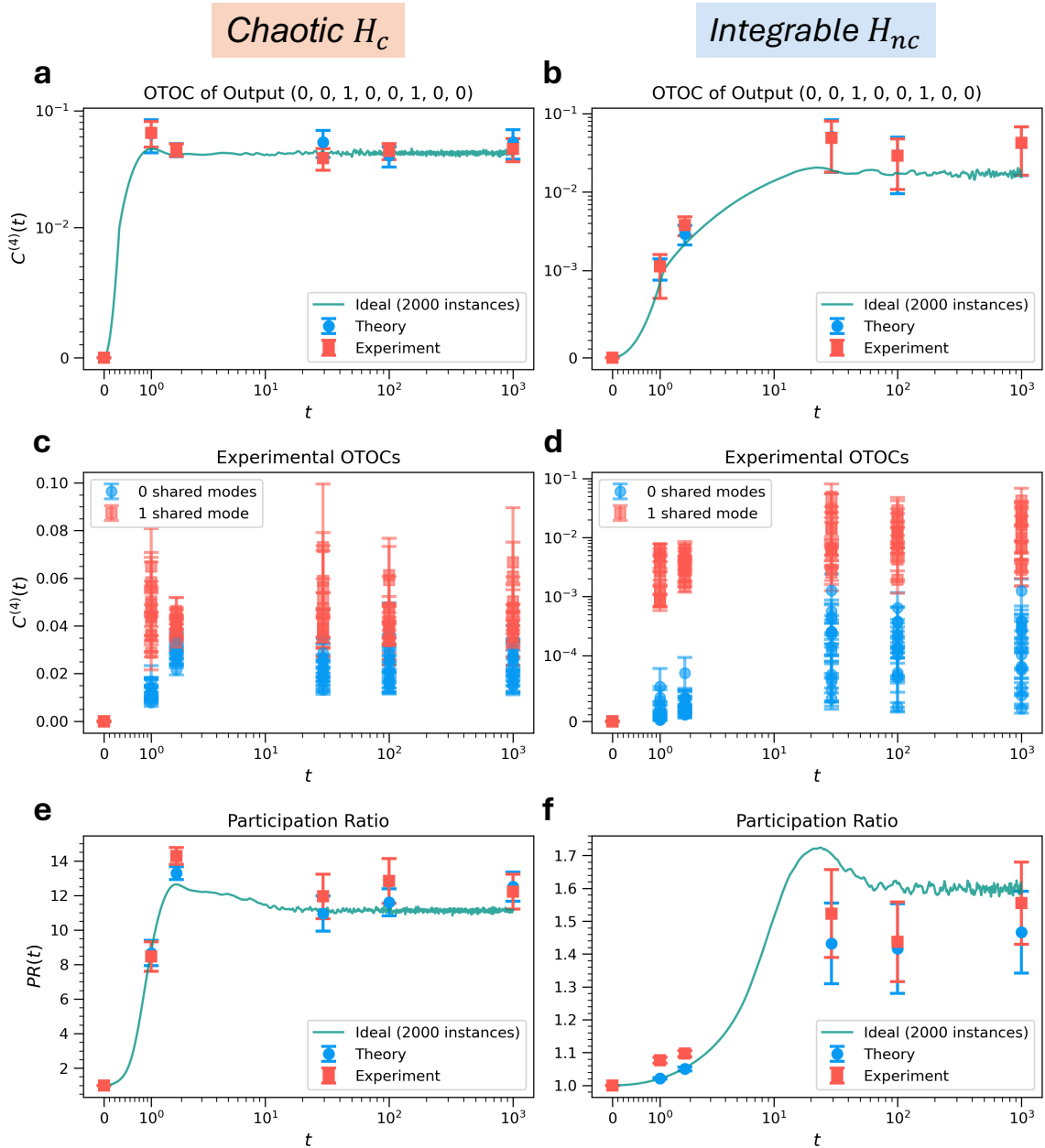


Fig. 4 Experimental results for the third chaos probe extracted from $\mathbf{p}(t)$. **a,b**, four-point OTOCs for the output configuration $|0_1, 0_2, 1_3, 1_4, 0_5, 0_6, 0_7, 0_8\rangle$ are shown for chaotic H_c and integrable H_{nc} . Experimental data are plotted in red, theoretical results assuming perfect Boson Sampling with the same unitaries in blue, and ideal curves averaged over 2000 instances in green. **c,d**, Experimental four-point OTOCs for H_c and H_{nc} are shown for all output configurations measured. Blue (red) points correspond to configurations with 0 (1) shared occupied modes with the input configuration. **e,f**, The participation ratios over all measured output configurations are shown for H_c and H_{nc} . Each data point represents the mean over all corresponding n_{t_k} realizations, with error bars denoting the standard error due to the finite number of instances.

evolution, these observables characterize bosonic delocalization rather than conventional many-body scrambling in interacting systems (although we retain the standard OTOC terminology for convenience).

To verify that the OTOC-equivalent observables capture signatures of quantum chaos, we first examine the temporal evolution of a representative output configuration. Figures 4a,b show the probability of observing the output state $|0_1, 0_2, 1_3, 0_4, 0_5, 1_6, 0_7, 0_8\rangle$ from the input state $|0_1, 0_2, 1_3, 1_4, 0_5, 0_6, 0_7, 0_8\rangle$, averaged over all realizations, for chaotic and integrable Hamiltonian

ensembles, respectively. Experimental results are compared with theoretical predictions obtained from the corresponding unitary ensembles, together with ideal curves averaged over a larger number of realizations. The close agreement between experiment and theory confirms that the measured boson sampling probabilities accurately reproduce the predicted OTOC-equivalent dynamics.

To obtain a more global picture, Figs. 4c,d show the averaged probabilities for all measured output configurations. The configurations are grouped according to the number of occupied modes shared with the initial state. This provides a natural measure of memory retention and information spreading: configurations with more shared modes preserve stronger information about the initial state, whereas those with fewer shared modes correspond to stronger scrambling. In both dynamical regimes, configurations sharing one mode with the input generally exhibit larger probabilities than those sharing none. The distinction lies in the degree to which this hierarchy is preserved. For chaotic dynamics, the difference between overlap sectors becomes less pronounced, indicating a more uniform redistribution of probability weight across the accessible Hilbert space and therefore stronger scrambling behavior. This overlap-sector dependence provides the signature for distinguishing chaotic and integrable dynamics. The observed behavior can be understood perturbatively, as configurations sharing more occupied modes with the input require fewer off-diagonal transitions and therefore exhibit larger probabilities at early times (see Appendix G for further details).

To characterize the global spreading behavior beyond individual output configurations, we consider the Participation Ratio (PR) [45, 46]

$$\text{PR}^{(l)}(t) = \frac{1}{\sum_{i=1}^D (p_i^{(l)}(t))^2}, \quad (10)$$

where the summation runs over all collision-free output configurations. The participation ratio measures the effective number of configurations contributing significantly to the output distribution. For example, a fully localized distribution gives $\text{PR} = 1$, whereas a completely delocalized distribution over D configurations approaches $\text{PR} \sim D$. Figs 4e,f show the ensemble-averaged PR as a function of time for chaotic and integrable dynamics. Clear differences can be observed between the two regimes. In the chaotic case, the participation ratio rapidly increases and reaches values around 12, indicating that probability weight spreads across a large fraction of the accessible configuration space. In contrast, the integrable case remains close to unity, with values around 1.6, reflecting a much stronger retention of probability within a limited subset of configurations. Experimental measurements show good agreement with theoretical predictions across the entire evolution. Therefore, PR provides an effective global measure of Hilbert-space delocalization and serves as an additional experimental signature for distinguishing chaotic and integrable dynamics. Additional theoretical and numerical analyses of these OTOC-equivalent observables are presented in Appendix G, where we show that chaotic dynamics exhibit distinct late-time fluctuation signatures in the temporal evolution of the output probabilities, whereas the short-time behavior follows a universal power-law scaling that is largely independent of the underlying dynamics.

These observations are consistent with the behavior identified in Sections 4.1 and 4.2. In particular, the growth and saturation of the PR coincide with the minimum of the PT distance $\mathcal{D}(t)$ and the peak of the Shannon entropy. Together, these three probes provide complementary perspectives on the same underlying dynamics: the Porter–Thomas distance characterizes the emergence of random-matrix behavior, the Shannon entropy quantifies probability delocalization, and the OTOC-equivalent observables capture information scrambling. Therefore, they provide a unified picture in which chaotic dynamics lead to rapid spreading of probability weight, reduced memory of the initial configuration, and enhanced scrambling across the accessible Hilbert space.

5 Discussion and Conclusion

From a theoretical perspective, the consistency among the three proposed probes suggests that different statistical quantities extracted from boson sampling outputs capture common signatures of the underlying chaotic dynamics. The Porter–Thomas distance characterizes the emergence of random-matrix behavior, the Shannon entropy quantifies Hilbert-space delocalization, and the OTOC-equivalent observables probe information scrambling. Although these probes capture different

physical aspects of the dynamics, they exhibit correlated temporal behavior and consistently identify the same underlying dynamical transition. Our results also establish an operational connection between boson sampling statistics and conventional measures of quantum chaos. If the underlying Hamiltonian is already believed to be chaotic, then boson sampling data can be used to estimate where the dynamics come closest to Haar-like behavior. In the language of spectral statistics, this gives experimental access to the time of the minimum of the spectral form factor, without having to reconstruct the full spectrum or to use time-reversal protocols. Hence, we show that multiphoton interference provides an operational way to locate the onset of strongest scrambling in a system whose microscopic dynamics may otherwise be difficult to characterize directly. Taken together, these results establish a direct correspondence between experimentally accessible boson sampling statistics and established probes of quantum chaos, providing a unified framework that connects spectral properties, information scrambling, and multiphoton interference.

From an experimental perspective, the programmable integrated photonic chip provides several advantages for probing quantum chaos. The reconfigurable architecture enables the implementation of large ensembles of unitary dynamics and access to time-dependent boson sampling statistics, making it possible to experimentally probe spectral properties, Hilbert-space delocalization, and information scrambling within a unified framework. Since boson sampling intrinsically relies on multiphoton interference and computationally complex output statistics, the proposed framework naturally inherits key advantages of photonic quantum information processing for accessing complex dynamical behavior. Finite system size and hardware imperfections, including loss and device nonidealities, primarily affect the sharpness of the asymptotic predictions while preserving the qualitative distinction between chaotic and integrable dynamics, consistent with both theoretical and experimental results. Numerical scaling results further indicate that these signatures become increasingly pronounced with increasing system size (see Appendix F), where larger systems are expected to provide stronger separation between ergodic and non-ergodic dynamics and enable more direct studies of information scrambling in higher-dimensional Hilbert spaces. These observations highlight the potential of integrated photonic boson sampling platforms for studying increasingly complex quantum dynamics.

Looking forward, although the present work focuses on a random-matrix Hamiltonian framework, the proposed approach is not restricted to this specific model. As discussed in Appendix C, the same framework can be naturally extended to more general many-body spin systems through the Holstein–Primakoff mapping in the dilute regime. The current implementation therefore serves as a proof-of-principle demonstration of a broader methodology for probing quantum chaos through boson sampling statistics. Beyond random-matrix dynamics, the proposed framework may enable future studies of a wider range of dynamical phenomena on programmable photonic platforms, including localization transitions, nonergodic behavior, and more general scrambling dynamics [47]. Since boson sampling has found applications in areas ranging from graph-theoretic problems to molecular vibronic spectra, our results further raise the question of whether the computational hardness arising in such problems is related to the same mechanisms of delocalization and information spreading that underlie quantum chaos. The present work provides a concrete experimental framework for systematically investigating these potential connections in future studies. More broadly, the present work highlights the potential of connecting multiphoton interference with signatures of complex quantum dynamics, providing new opportunities for studying nonequilibrium quantum physics and information dynamics in larger quantum systems.

In conclusion, we proposed and experimentally demonstrated a boson sampling-based framework for probing quantum chaos on a programmable integrated photonic platform. Theoretically, we establish an operational connection between boson sampling statistics and conventional signatures of quantum chaos, enabling experimentally accessible probes of spectral properties, Hilbert-space delocalization, and information scrambling directly from measured output distributions. Experimentally, we realize these ideas on an eight-mode silicon photonic processor with two indistinguishable photons, combining arbitrary unitary programming and multiphoton correlation measurements within a scalable integrated architecture. Using three complementary probes extracted from boson sampling statistics, we show that chaotic and integrable dynamics exhibit clearly distinguishable signatures. The proximity to Porter–Thomas statistics reveals the emergence of Haar-like behavior and characteristic features of the spectral form factor; the Shannon entropy captures enhanced probability spreading, and Hilbert-space delocalization; and the OTOC-equivalent observables characterize

stronger information scrambling and reduced memory retention in chaotic systems. Experimental results show good agreement with theoretical predictions and consistently distinguish chaotic and integrable dynamics across all measured observables. Our work establishes boson sampling as a practical tool for studying quantum chaos and demonstrates the potential of integrated photonic platforms for investigating complex quantum dynamics. More broadly, the proposed framework provides new opportunities for exploring nonequilibrium quantum physics, information dynamics, and related phenomena in larger programmable quantum systems.

Acknowledgements

L.C.K. acknowledges support from the National Research Foundation, Singapore, and the Ministry of Education, Singapore. K.H.L. acknowledges the Plan France 2030 through the project NISQ2LSQ (Grant ANR-22-PETQ-0006), the project OQuLus (Grant ANR-22-PETQ-0013), and also the CNRS@CREATE internal grant NGAP (NRF2023-ITC004-001). N.T.W.K. is supported by the CQT NQSS PhD scholarship. K.C. gratefully acknowledges the Milner Foundation for their support. K.H.L. would like to thank Dariel Mok Wai-Keong for helpful discussions.

Author contributions

All authors contributed to the conception of the work. Y.C.Z. designed the chip, built the experimental setup, and performed the experiments. K.H.L., K.C., and N.T.W.K. equally contributed to the theoretical derivations, calculations, and simulations. H.Z. and L.X.W. assisted with the experiments, and V.M.B. assisted with the theoretical analysis. S.C., A.Q.L., Y.O., and L.C.K. supervised and coordinated all the work. Y.C.Z., K.H.L., K.C., and N.T.W.K. wrote the manuscript with contributions from all co-authors.

Data availability

The data supporting the findings of this study are available from the corresponding author on reasonable request.

Competing interests

The authors declare no competing interests.

Additional information

The Appendix is available for this paper.

References

- [1] Ekert, A. K. *et al.* Direct estimations of linear and nonlinear functionals of a quantum state. *Physical review letters* **88**, 217901 (2002).
- [2] Nielsen, M. A. & Chuang, I. L. *Quantum computation and quantum information* (Cambridge university press, 2010).
- [3] Bennett, C. H. & DiVincenzo, D. P. Quantum information and computation. *Nature* **404**, 247–255 (2000).
- [4] Zhang, G. *et al.* An integrated silicon photonic chip platform for continuous-variable quantum key distribution. *Nature Photonics* **13**, 839–842 (2019).
- [5] Gisin, N., Ribordy, G., Tittel, W. & Zbinden, H. Quantum cryptography. *Reviews of modern physics* **74**, 145 (2002).

- [6] Pirandola, S. *et al.* Advances in quantum cryptography. *Advances in optics and photonics* **12**, 1012–1236 (2020).
- [7] Zhan, Y. *et al.* Loop quantum photonic chip for coherent multi-time-step evolution. *Laser & Photonics Reviews* e02699 (2026).
- [8] Georgescu, I. M., Ashhab, S. & Nori, F. Quantum simulation. *Reviews of Modern Physics* **86**, 153–185 (2014).
- [9] Luo, W. *et al.* Recent progress in quantum photonic chips for quantum communication and internet. *Light: Science & Applications* **12**, 175 (2023).
- [10] Lenzini, F. *et al.* Integrated photonic platform for quantum information with continuous variables. *Science advances* **4**, eaat9331 (2018).
- [11] Wang, J., Sciarrino, F., Laing, A. & Thompson, M. G. Integrated photonic quantum technologies. *Nature photonics* **14**, 273–284 (2020).
- [12] Flamini, F., Spagnolo, N. & Sciarrino, F. Photonic quantum information processing: a review. *Reports on Progress in Physics* **82**, 016001 (2018).
- [13] Zhang, H. *et al.* Integrated photonic quantum computing: From silicon to lithium niobate. *arXiv preprint arXiv:2601.16484* (2026).
- [14] Zhan, Y. *et al.* Physics-aware analytic-gradient training of photonic neural networks. *Laser & Photonics Reviews* **18**, 2300445 (2024).
- [15] Zhang, H. *et al.* An optical neural chip for implementing complex-valued neural network. *Nature communications* **12**, 457 (2021).
- [16] Zhu, H. H. *et al.* Large-scale photonic network with squeezed vacuum states for molecular vibronic spectroscopy. *Nature communications* **15**, 6057 (2024).
- [17] Zhang, H. *et al.* Resource-efficient high-dimensional subspace teleportation with a quantum autoencoder. *Science advances* **8**, eabn9783 (2022).
- [18] D’Alessio, L., Kafri, Y., Polkovnikov, A. & Rigol, M. From quantum chaos and eigenstate thermalization to statistical mechanics and thermodynamics. *Advances in Physics* **65**, 239–362 (2016).
- [19] Cotler, J., Hunter-Jones, N., Liu, J. & Yoshida, B. Chaos, complexity, and random matrices. *Journal of High Energy Physics* **2017**, 48 (2017).
- [20] García-Mata, I., Jalabert, R. A. & Wisniacki, D. A. Out-of-time-order correlators and quantum chaos. *arXiv preprint arXiv:2209.07965* (2022).
- [21] Maldacena, J., Shenker, S. H. & Stanford, D. A bound on chaos. *Journal of High Energy Physics* **2016**, 106 (2016).
- [22] Gärttner, M. *et al.* Measuring out-of-time-order correlations and multiple quantum spectra in a trapped-ion quantum magnet. *Nature Physics* **13**, 781–786 (2017).
- [23] Mi, X. *et al.* Information scrambling in quantum circuits. *Science* **374**, 1479–1483 (2021).
- [24] Li, J. *et al.* Measuring out-of-time-order correlators on a nuclear magnetic resonance quantum simulator. *Phys. Rev. X* **7**, 031011 (2017).
- [25] Chávez-Carlos, J. *et al.* Quantum and classical lyapunov exponents in atom-field interaction systems. *Phys. Rev. Lett.* **122**, 024101 (2019).

- [26] Yu, S. *et al.* A von-neumann-like photonic processor and its application in studying quantum signature of chaos. *Light: Science & Applications* **13**, 74 (2024).
- [27] Lemos, G. B., Gomes, R. M., Walborn, S. P., Souto Ribeiro, P. H. & Toscano, F. Experimental observation of quantum chaos in a beam of light. *Nature communications* **3**, 1211 (2012).
- [28] Wang, J. *et al.* Many-body quantum chaos, localization, and multiphoton entanglement in optical synthetic frequency dimension. *Phys. Rev. Appl.* **23**, 034076 (2025).
- [29] Madsen, L. S. *et al.* Quantum computational advantage with a programmable photonic processor. *Nature* **606**, 75–81 (2022).
- [30] Brod, D. J. *et al.* Photonic implementation of boson sampling: a review. *Advanced Photonics* **1**, 034001–034001 (2019).
- [31] Spring, J. B. *et al.* Boson sampling on a photonic chip. *Science* **339**, 798–801 (2013).
- [32] Zhu, H. *et al.* GBS-assisted quantum unsupervised machine learning on a universal programmable integrated quantum chip. *Research* **8**, 1006 (2025).
- [33] Huh, J., Guerreschi, G. G., Peropadre, B., McClean, J. R. & Aspuru-Guzik, A. Boson sampling for molecular vibronic spectra. *Nature Photonics* **9**, 615–620 (2015).
- [34] Deng, Y.-H. *et al.* Solving graph problems using gaussian boson sampling. *Phys. Rev. Lett.* **130**, 190601 (2023).
- [35] Hoch, F. *et al.* Quantum machine learning with adaptive boson sampling via post-selection. *Nature Communications* **16**, 902 (2025).
- [36] Wang, X.-W. *et al.* Experimental boson sampling enabling cryptographic one-way function. *Physical Review Letters* **130**, 060802 (2023).
- [37] Boixo, S. *et al.* Characterizing quantum supremacy in near-term devices. *Nature Physics* **14**, 595–600 (2018).
- [38] Porter, C. E. & Thomas, R. G. Fluctuations of nuclear reaction widths. *Phys. Rev.* **104**, 483–491 (1956).
- [39] Shannon, C. E. A mathematical theory of communication. *The Bell system technical journal* **27**, 379–423 (1948).
- [40] Bastidas, V. M. *et al.* Equilibration of noninteracting photons and quantum signatures of chaos. *Phys. Rev. B* **112**, 134304 (2025).
- [41] Lenz, G., Życzkowski, K. & Saher, D. Scaling laws of the additive random-matrix model. *Phys. Rev. A* **44**, 8043–8050 (1991).
- [42] Chavda, N. D., Deota, H. N. & Kota, V. K. B. Poisson to goe transition in the distribution of the ratio of consecutive level spacings. *Physics Letters A* **378**, 3012–3017 (2014).
- [43] Clements, W. R., Humphreys, P. C., Metcalf, B. J., Kolthammer, W. S. & Walmsley, I. A. Optimal design for universal multiphoton interferometers. *Optica* **3**, 1460–1465 (2016).
- [44] Panaretos, V. M. & Zemel, Y. Statistical aspects of wasserstein distances. *Annual Review of Statistics and Its Application* **6**, 405–431 (2019).
- [45] Borgonovi, F., Izrailev, F. M. & Santos, L. F. Timescales in the quench dynamics of many-body quantum systems: Participation ratio versus out-of-time ordered correlator. *Phys. Rev. E* **99**, 052143 (2019).

- [46] Bastidas, V. M., Estarellas, M. P., Osada, T., Nemoto, K. & Munro, W. J. Quantum metamorphism. *Phys. Rev. B* **102**, 224307 (2020).
- [47] Kulkarni, A. V., Tiwari, V., Sharma, A. & Raina, A. Photonic simulation of localization phenomena using boson sampling. *Phys. Rev. A* **111**, 032622 (2025).
- [48] Curtiss, J. H. On the Distribution of the Quotient of Two Chance Variables. *The Annals of Mathematical Statistics* **12**, 409 – 421 (1941).
- [49] Aaronson, S. & Arkhipov, A. The computational complexity of linear optics (2011). Proceedings of the forty-third annual ACM symposium on Theory of computing.
- [50] Spagnolo, N. *et al.* General rules for bosonic bunching in multimode interferometers. *Phys. Rev. Lett.* **111**, 130503 (2013).
- [51] Peropadre, B., Aspuru-Guzik, A. & García-Ripoll, J. J. Equivalence between spin hamiltonians and boson sampling. *Phys. Rev. A* **95**, 032327 (2017).
- [52] Fortes, E. M., García-Mata, I., Jalabert, R. A. & Wisniacki, D. A. Gauging classical and quantum integrability through out-of-time-ordered correlators. *Phys. Rev. E* **100**, 042201 (2019).
- [53] Omanakuttan, S., Chinni, K., Blocher, P. D. & Poggi, P. M. Scrambling and quantum chaos indicators from long-time properties of operator distributions. *Phys. Rev. A* **107**, 032418 (2023).

Appendix A Conditional Probabilities and Photon-Number Detection

In this appendix, we clarify the definition of the probability distributions used in the main text and their relation to the experimental detection scheme.

A.1 Experimental Detection and Post-Selection

In an ideal boson sampling experiment with photon-number-resolving detectors, one would have access to the full set of output configurations, including events where multiple photons occupy the same mode (collisions). For a system with M modes and N photons, the total number of possible output configurations is

$$N_0 = \binom{M + N - 1}{N}. \quad (\text{S1})$$

In our experiment, we consider $M = 8$ modes and $N = 2$ photons, giving

$$N_0 = \binom{9}{2} = 36. \quad (\text{S2})$$

However, due to the use of non-number-resolving detectors, we restrict attention to events in which the number of detected photons matches the number of injected photons, and in which no two photons occupy the same output mode. This corresponds to selecting the subset of *collision-free* outcomes, whose number is

$$D = \binom{M}{N} = \binom{8}{2} = 28. \quad (\text{S3})$$

A.2 Conditional Probability Distribution

Let p_j denote the ideal probability of observing output configuration j , including both collision-free and collision events. Since we only retain collision-free outcomes, we work with the conditional probability distribution defined by

$$p_j^{\text{cond}} = \frac{p_j}{\sum_{k \in \mathcal{C}} p_k}, \quad j \in \mathcal{C}, \quad (\text{S4})$$

where \mathcal{C} denotes the set of collision-free configurations. This normalization ensures that the probabilities sum to one over the experimentally accessible subset:

$$\sum_{j \in \mathcal{C}} p_j^{\text{cond}} = 1. \quad (\text{S5})$$

A.3 Relation to the Main Text

In the main text, the probability vectors $\mathbf{p}^{(l)}(t)$ should be interpreted as conditional distributions over collision-free outcomes:

$$\mathbf{p}^{(l)}(t) = \left(p_1^{(l)}(t), \dots, p_D^{(l)}(t) \right), \quad (\text{S6})$$

where

$$D = \binom{M}{N}. \quad (\text{S7})$$

All quantities defined in Section 4, including the empirical distribution $f_t(p)$, the Wasserstein distance $\mathcal{D}(t)$, the Shannon entropy $S_{\text{avg}}(t)$, and the participation ratio $\text{PR}(t)$, are computed using these conditional probability distributions.

In the following, we show in detail that the probability distribution of the conditional probabilities follows the Porter–Thomas distribution when we perform boson sampling on a Haar-random unitary U ; that is, we show that $\text{Probability}(p_j^{\text{cond}} \in [p, p + dp]) \approx D e^{-Dp} dp$ when $(N_0 - D)/N_0 \approx 0$. Since

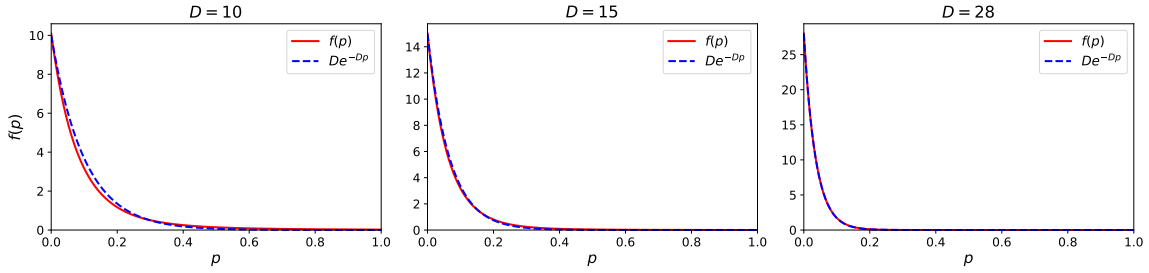


Fig. S1 $f(p)$ plots for various values of D . Here, we show that for $N_0 = 36$ and $D = 28$ that p_j^{cond} follows the Porter–Thomas distribution perfectly, which justifies why we use the Porter–Thomas distribution instead of the actual distribution of p_j^{cond} in our work. We also show that for smaller values of D , this approximation (see Eq. S9) of p_j^{cond} by the Porter–Thomas distribution breaks down.

U is a Haar random unitary, we know that the probability distribution of p_j is the Porter–Thomas distribution. Thus, the probability distribution of $Y = 1 - \sum_{x \in C} p_x$ is given by

$$\text{Probability}(Y \in [y, y + dy]) = \frac{N_0^C (1 - y)^{C-1} e^{-N_0(1-y)}}{(C - 1)!}, \quad (\text{S8})$$

where we define $C = N_0 - D$ and use the fact that a sum of exponential random variables is a Gamma distribution. Then, we notice that p_j^{cond} is essentially a ratio distribution between the Porter–Thomas distribution in p_j and the Gamma distribution of Y . Thus, if we let $f(p)$ be the probability distribution of p_j^{cond} , we have, using the methods in [48], the following equation

$$f(p) = \int_0^1 dy y N_0 e^{-N_0 p y} \frac{N_0^C (1 - y)^{C-1} e^{-N_0(1-y)}}{(C - 1)!} \quad (\text{S9a})$$

$$\approx D e^{-Dp}, \quad (\text{S9b})$$

where the approximation to a Porter–Thomas distribution in the last line is better for smaller values of $(N_0 - D)/N_0$.

To illustrate this, we consider the case where $N_0 = 36$ and various values of D in Fig. S1. Note that $N_0 = 36$ is the full state space of a Boson Sampling experiment with 2 input photons and with photon number resolving detectors, and $D = 28$ corresponds to our situation where we discard the cases where we see only 1 detector click, which corresponds to the events where two photons exit from the same mode. As can be seen, for small values of D , the approximation is poor. On the other hand, for $D = 28$, the approximation is essentially perfect. This justifies the use of the conditional probabilities in the Shannon Entropy formula. This also means that if our photonic chip size is too small, for example if we were working with a three-mode photonic chip, then we cannot use the Porter–Thomas distribution for p_j^{cond} when we neglect the events where two photons exit from the same mode, since the number of those events (which is 3 in this case) is equal to the number of events that have two detector clicks.

A.4 Remarks

The use of conditional probabilities reflects a standard experimental constraint in photonic boson sampling. While this restriction modifies the full output distribution, the statistical diagnostics considered in this work remain well-defined and robust, as they depend only on the relative distribution of probability weight across the accessible configurations. A more complete treatment including collision events would require photon-number-resolving detectors, but is not expected to qualitatively change the distinctions observed between chaotic and integrable dynamics in the present setting.

Appendix B Construction of Unitaries to Study Integrable to Chaos Transition

In our experiments, we sampled 16 matrices for H_0 and for V and used the same matrices to construct $H_{\text{nc}} = H_{\Lambda=0.01}$ and $H_c = H_{\Lambda=1000}$. The chosen values of Λ ensure that H_c , H_{nc} generates chaotic and integrable dynamics respectively [42]. Then, we used the matrices sampled to construct the unitaries $e^{-iH_c t_i}$ and $e^{-iH_{\text{nc}} t_i}$ for $t_i = t_1, t_3, t_4, t_5$. For $t = t_2$, we repeated the above procedure but we sampled 75 matrices for H_0 and V for H_c and 16 matrices for H_0 and V for H_{nc} . Here, the values t_i selected are $[t_1, t_2, t_3, t_4, t_5] = [1, 1.79, 29.29, 100, 1000]$, and are chosen so as to see the behavior of $e^{-iH_\Lambda t}$ across a wide range of time values. We sampled more matrices for $t = t_2$ for H_c as it is a theoretically important point, being the point at which the 4-point SFF of H_c reaches a minimum. The importance of $t = t_2$ for H_c is explained in Section 2.2.

After we have constructed the many realizations of the unitary matrices $e^{-iH_c t_i}$ and $e^{-iH_{\text{nc}} t_i}$ for the values of t_i chosen, we put these on our 8-mode photonic chip using the procedure described in Appendix D.5, and then performed boson sampling following the procedure described in Appendix D.1. In the end, for $t = t_1, t_3, t_4, t_5$, we obtained 16 sets of probability distributions for H_c and H_{nc} , and for $t = t_2$, we obtained 16 and 75 sets of probability distributions corresponding to $e^{-iH_{\text{nc}} t_i}$ and $e^{-iH_c t_i}$ respectively.

Appendix C Generalization to Spin Hamiltonians

While we have considered a random matrix model H_Λ in this paper, the framework also extends to a large class of many-body spin Hamiltonians. Consider the following spin Hamiltonian:

$$H_s = \sum_{i,j=1}^K S_i H_{ij} S_j^\dagger, \quad (\text{S10})$$

where H_{ij} are matrix elements of a Hermitian matrix and S_i is the spin-1/2 lowering operator on the i th spin. Clearly, H commutes with the total magnetization $M = \sum_{i=1}^K S_i^z$, S_i^z being the operator that represents the projection of the i th spin onto the z axis. Then, we recall that the Holstein–Primakoff transformation,

$$S_i = a_i^\dagger \sqrt{1 - a_i^\dagger a_i} \quad (\text{S11a})$$

$$S_i^z = \frac{1}{2} - a_i^\dagger a_i, \quad (\text{S11b})$$

converts H_s into a bosonic Hamiltonian H_b ,

$$H_b = \sum_{i,j=1}^K H_{ij} a_i^\dagger (1 - a_i^\dagger a_i) a_j, \quad (\text{S12})$$

and also converts the corresponding dynamics arising from $e^{-iH_s t}$ in the m magnetisation subspace to the corresponding dynamics due to $e^{-iH_b t}$ in the subspace with $N = K/2 - m$ photons. Now, recall that for Boson Sampling experiments where $K \gg N^2$, the probability of observing two or more photons in the same mode is vanishingly low for typical unitaries (as K increases) [49–51]. Hence, by choosing $K \gg N^2$, we have $a_i^\dagger \sqrt{1 - a_i^\dagger a_i} \approx a_i^\dagger$ for such Boson Sampling experiments. Hence, we have $H_s \xrightarrow{\text{Holstein-Primakoff}} H_b \approx \sum_{i,j} H_{ij} a_i^\dagger a_j$, which means we can perform Boson Sampling with N input photons on $e^{-iH_b^{\text{exc}} t}$ to probe the presence of chaos in H_s in the m -magnetisation subspace, where H_b^{exc} is H_b projected onto the one-excitation subspace, represented by a $K \times K$ matrix. Note that the condition $K \gg N^2$ is not especially restrictive, since it is exactly the condition that is required for Boson Sampling to be classically intractable [49].

Appendix D Experimental Detail

D.1 Experimental Procedure

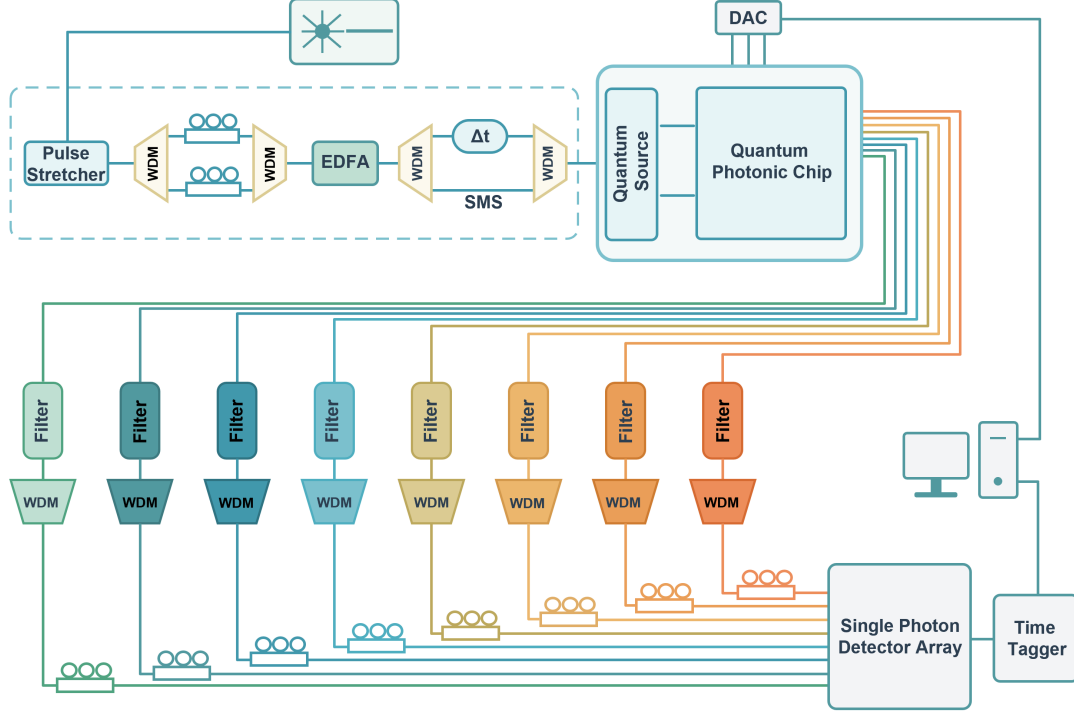


Fig. S2 The experimental setup for the integrated photonic circuit experiment. Schematic of the optical source, programmable photonic chip, and photon detection system used for the quantum chaos experiments.

The experimental setup for the quantum chaos study is illustrated in Fig. S2. The process involves both an input and output light path, with precise control to ensure high-quality photon generation and detection.

The pump light is generated using an ultrafast optical clock device. To expand the light's bandwidth to approximately 10 nm, the pump light is first directed through a pulse compressor. This broad bandwidth is then narrowed by passing the light through a 100G Wavelength Division Multiplexing (WDM) device, which isolates the 1550 nm wavelength with a resolution of 0.5 nm. Following this, a wavelength filter is employed to further refine the linewidth and suppress background noise. The filtered light is then amplified using an erbium-doped fiber amplifier, boosting its power to approximately 100 mW. However, the amplification process also introduces additional background noise, which necessitates further noise suppression. A second set of WDM devices and wavelength filters is applied to minimize noise while maintaining the desired wavelength's power. To ensure that the optical paths are equalized, tunable fiber delay lines are introduced in one of the channel arms. This adjustment compensates for any discrepancies in the optical path lengths, ensuring synchronized photon arrival. Additionally, polarization controllers are placed in the input path to align the input light mode with the coupling structure. Finally, the prepared pump light is coupled into the photonic chip through fiber grating arrays, which serve as the interface between the external optical system and the on-chip waveguides. The pump light interacts with the integrated photonic structures to generate and manipulate quantum states according to the experimental algorithm.

After completing the computation within the photonic chip, the output photons are guided through a second set of WDM devices and filters to isolate the desired wavelength and further suppress noise. A polarization controller is placed in the output path to adjust the polarization mode of

the outgoing light, ensuring compatibility with the detection system. The filtered photons are then detected using SNSPDs, which convert the photon signals into electrical signals with high sensitivity and low noise. These electrical signals are processed by a time-tagger, which records the precise timing of each detected photon. The timing data is subsequently transmitted to a computer, which controls the photonic chip’s reconfigurable components. The computer interfaces with the photonic chip via a DAC. The DAC modulates the heating elements on the chip, altering the optical path lengths and reconfiguring the circuit for the next measurement round.

D.2 Chip Calibration

The calibration procedure determines the relationship between heater power and adjustable phases for each MZI. We first consider the calibration of the phase shifter placed between two beam splitters. When light enters the top arm of the MZI, the output state P at the two ports can be expressed as:

$$P = \mathcal{T} \cdot \begin{bmatrix} 1 \\ 0 \end{bmatrix} = ie^{i\frac{\theta}{2}} \begin{bmatrix} \sin \frac{\theta}{2} \\ \cos \frac{\theta}{2} \end{bmatrix}, \quad (\text{S13})$$

where the output power distribution depends on the induced phase change θ . This relationship allows interference fringes to be observed as the phase is varied.

The phase shift θ originates from the optical path difference caused by a change in the effective refractive index. Thermal phase shifting is achieved by heating a titanium nitride resistor integrated with the waveguide, resulting in a temperature-induced refractive index change proportional to the heater power:

$$\theta = \frac{L}{\lambda} \cdot k \cdot P_{\text{heater}} + \theta_0, \quad (\text{S14})$$

where L denotes the waveguide length influenced by the heater, λ is the wavelength, θ_0 is an intrinsic phase offset due to fabrication imperfections, P_{heater} represents the heater power, and k is a proportionality coefficient relating heater power to refractive index modulation.

Experimentally, we systematically vary the heater power applied to the MZI and measure the resulting output power variation. A fitting procedure is then employed to determine the coefficients k and θ_0 . This calibration enables precise control of the phase shifts using heater power settings.

D.3 Photon source characterization

The photon source is first characterized under the degenerate spontaneous four-wave mixing process. The spectral properties of the pump laser are measured using an optical spectrum analyzer (OSA). The initial broadband pump exhibits a spectral bandwidth of approximately 1.9 nm. To improve the spectral purity and suppress background noise, a 100 GHz wavelength division multiplexer (WDM) is employed, which reshapes the pump spectrum to a narrower bandwidth of approximately 0.7 nm.

Two specific wavelength channels, centered at 1553.33 nm and 1546.92 nm, are selected from the broadband pump using the WDM. Through the degenerate SFWM process in the spiral waveguide, correlated photon pairs are generated with identical wavelengths centered at 1550.12 nm. To further characterize the spectral correlations of the generated photon pairs, we measure the joint spectral intensity (JSI). In the experiment, the spiral waveguide operates under a single-pump configuration, and the generated photon pairs are directly routed into a 100 GHz WDM for spectral filtering. The signal and idler wavelength ranges are discretized into five channels each, covering 1544.5–1547.7 nm for the signal and 1552.5–1555.7 nm for the idler.

Coincidence measurements are performed across all possible combinations of these discretized wavelength channels, resulting in a total of 25 measurement points. The collected coincidence counts are subsequently normalized to reconstruct the JSI, providing a quantitative evaluation of the spectral correlation and purity of the photon source.

D.4 Sources of Error

In this section, we analyze the primary sources of experimental imperfections that affect the performance of the on-chip boson sampling system and the accuracy of quantum chaos diagnostics. These

errors mainly arise from photon source non-idealities, imperfect optical transformations, measurement noise, and multiphoton contributions.

Photon source imperfections from SFWM in Si waveguides. Photon pairs are generated via SFWM in silicon waveguides. Ideally, the generated two-photon state should be spectrally factorable and indistinguishable across different sources. However, in practice, residual spectral correlations in the joint spectral amplitude lead to partial distinguishability between photons.

This distinguishability reduces the degree of multiphoton interference, which is essential for boson sampling. As a result, the output probability distribution deviates from the ideal bosonic distribution and tends toward a classical distribution. In the context of quantum chaos characterization, such imperfections can suppress signatures of chaotic behavior, for example by reducing the agreement with the Porter–Thomas distribution and lowering the measured Shannon entropy.

Imperfections in MZI-based unitary transformations. The programmable linear optical network is implemented using cascaded MZIs controlled by thermo-optic phase shifters. Fabrication imperfections and thermal cross-talk introduce deviations from the target unitary transformation.

Specifically, phase errors arising from heater non-uniformity, limited calibration precision, and thermal drift result in inaccurate setting of the MZI phases. These errors accumulate across the interferometer mesh and lead to a deviation between the implemented unitary and the ideal unitary. Such unitary errors distort the output photon distribution and reduce the fidelity of the boson sampling process. In quantum chaos analysis, this may lead to incorrect identification of statistical properties, such as deviations from GOE behavior or artificial broadening of the output distribution.

Noise photons in the measurement system. Noise photons originating from imperfect pump suppression, Raman scattering, and detector dark counts contribute to the measured coincidence events. Although spectral filtering (e.g., WDM and AMZI) is applied to suppress residual pump light, incomplete filtering introduces background counts. These noise photons degrade the signal-to-noise ratio and introduce spurious detection events, which bias the reconstructed output distribution. In particular, noise can artificially increase entropy-like measures and obscure the statistical features used to distinguish chaotic and integrable regimes.

D.5 Chip decomposition for Boson Sampling

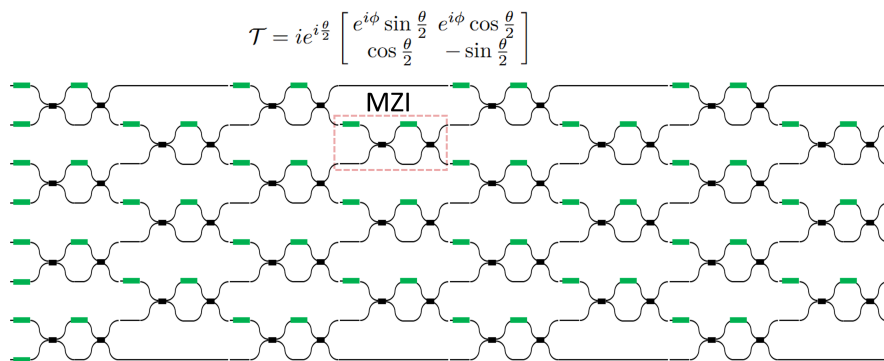


Fig. S3 Chip decomposition for boson sampling. Schematic of the programmable MZI mesh architecture used to realize arbitrary unitary transformations for boson sampling experiments.

We propose an arrangement of beam splitters and phase shifters for constructing universal multiport interferometers, which serve as the arbitrary unitaries in the boson sampling algorithm, as shown in Fig. S3. This design allows each mode to interact with its nearest neighbor, creating a compact and symmetrical structure that optimizes space and efficiency.

Each fundamental transformation within the MZI unit is governed by two-phase shift parameters, θ and ϕ , and is defined as follows,

$$\mathcal{T} = ie^{i\frac{\theta}{2}} \begin{bmatrix} e^{i\phi} \sin \frac{\theta}{2} & e^{i\phi} \cos \frac{\theta}{2} \\ \cos \frac{\theta}{2} & -\sin \frac{\theta}{2} \end{bmatrix}. \quad (\text{S15})$$

Each MZI operation can be represented by a unitary transformation matrix, denoted by T_{ij} , of the form:

$$T_{ij} = \begin{bmatrix} 1 & \cdots & & & \\ \vdots & a_{i,i} & a_{i,j} & & \\ & a_{j,i} & a_{j,j} & \vdots & \\ & & \cdots & \ddots & \\ & & & & 1 \end{bmatrix}_N. \quad (\text{S16})$$

The parameters of the $T_{i,j}$ matrices determine the values of the beam splitters and phase shifts corresponding to Eq. S15. We show that an arbitrary $N \times N$ unitary matrix can be decomposed into $N(N-1)/2$ MZI units arranged in a specific sequence. Repeating this procedure iteratively yields the full target unitary. For additional details on the decomposition method, see our previous work [14].

Appendix E Theoretical Justification for Eq. 4 and Eq. 6

In this appendix, we provide a theoretical justification for the behavior of the distance \mathcal{D} (Eq. 4) from the Porter–Thomas distribution and the Shannon entropy, based on connections between spectral statistics, unitary designs, and boson sampling.

E.1 Spectral Form Factor and Frame Potential

For an ensemble of unitary operators $\{U(t)\} = \{e^{-iHt}\}$, the k -th frame potential $\mathcal{F}_k(t)$ provides a measure of how close the ensemble is to forming a unitary k -design. Smaller values of $\mathcal{F}_k(t)$ indicate closer approximation to Haar-random unitaries, with the Haar ensemble achieving the minimum value $\mathcal{F}_k(t) = k!$. For ensembles of random matrix Hamiltonians (e.g., GOE), it is known that the $2k$ -point spectral form factor (SFF), denoted $(\mathcal{R}_{2k})^2$, is related to the frame potential via

$$F_k(t) \propto (\mathcal{R}_{2k}(t))^2, \quad (\text{S17})$$

up to normalization factors (see Ref. [19]). In chaotic systems, the SFF typically exhibits a dip-ramp-plateau structure: it decreases at early times, reaches a minimum at a characteristic time t^* , and then approaches a plateau at late times. This behavior implies that the unitary ensemble $\{e^{-iHt}\}$ is closest to a unitary design near $t \approx t^*$, and hence most closely approximates Haar-random behavior at that time.

E.2 Connection to Porter–Thomas Statistics

Boson sampling with Haar-random unitaries produces output probabilities that follow the Porter–Thomas distribution

$$P_{\text{PT}}(p) = D e^{-Dp}, \quad (\text{S18})$$

where D is the dimension of the Hilbert space. Therefore, if the ensemble $\{e^{-iHt}\}$ approximates a unitary design at time t , we expect the corresponding boson sampling output probabilities to be close to Porter–Thomas distributed. This motivates defining the distance

$$\mathcal{D}(t) = W_1(f_t(p), P_{\text{PT}}(p)), \quad (\text{S19})$$

as in Eq. 4, where $f_t(p)$ is the empirical distribution of probability values. Based on the above reasoning, we expect $\mathcal{D}(t)$ to exhibit a dip near $t \approx t^*$, corresponding to the minimum of the SFF. At later times, the distance approaches a plateau. We emphasize that, due to finite system size and limited sampling, this correspondence should be interpreted qualitatively rather than as an exact equality.

E.3 Entropy at the Haar Point

At times when $U(t)$ is close to Haar-random, the output probability distribution is approximately uniformly random over the simplex. In this case, one can compute the expected Shannon entropy. Let p_1, \dots, p_N be the probabilities associated with all output configurations (here $N \equiv D$). The Shannon entropy is

$$S = - \sum_{i=1}^N p_i \ln p_i . \quad (\text{S20})$$

The ensemble average over Haar-random unitaries is given by

$$\langle S \rangle_{\text{ens}} = \sum_{i=1}^N \left\langle p_i \ln \left(\frac{1}{p_i} \right) \right\rangle_{\text{ens}} . \quad (\text{S21})$$

Using the fact that the distribution of a single probability under the Haar measure is

$$P(p) = (N-1)(1-p)^{N-2} , \quad (\text{S22})$$

we obtain

$$\langle S \rangle_{\text{ens}} = \sum_{i=1}^N \int_0^1 dp p \ln \left(\frac{1}{p} \right) (N-1)(1-p)^{N-2} . \quad (\text{S23})$$

Evaluating the integral gives

$$\langle S \rangle_{\text{ens}} = -1 + \sum_{i=1}^N \frac{1}{i} . \quad (\text{S24})$$

Note that in the large- N limit, we can approximate

$$(1-p)^{N-2} \approx e^{-Np} , \quad (\text{S25})$$

which is the Porter–Thomas distribution, which yields

$$\langle S \rangle_{\text{ens}} \approx \sum_{i=1}^N \int_0^\infty dp p \ln \left(\frac{1}{p} \right) N e^{-Np} \quad (\text{S26})$$

$$= -1 + \ln(N) + \gamma, \quad (\text{S27})$$

where γ is the Euler-Mascheroni constant. In the main text, we use Eq. S24.

E.4 Connection to Experimental Observables

In our experiment, the quantity $S_{\text{avg}}(t)$ defined in Eq. 6 serves as an estimator for $\langle S \rangle_{\text{ens}}$. By the Central Limit Theorem, we expect that for sufficiently large ensembles,

$$S_{\text{avg}}(t) \approx \langle S \rangle_{\text{ens}} . \quad (\text{S28})$$

On the other hand, as the Hilbert-space dimension increases, concentration-of-measure results (e.g., Lévy’s lemma) imply that, when the unitary ensemble is close to Haar random, a typical realization satisfies

$$S \approx \langle S \rangle_{\text{ens}}, \quad (\text{S29})$$

independently of the particular probabilities $\{p_i\}_i$ used to calculate S . Hence, for small dimensions, one may improve the estimate by increasing the ensemble size, whereas for sufficiently large dimensions, and when the unitary ensemble is close to Haar random, even a single random matrix is expected to yield a value close to the ensemble average. In both cases, we expect the entropy to reach its maximum near the same time t^* at which $\mathcal{D}(t)$ is minimized and the SFF reaches its dip.

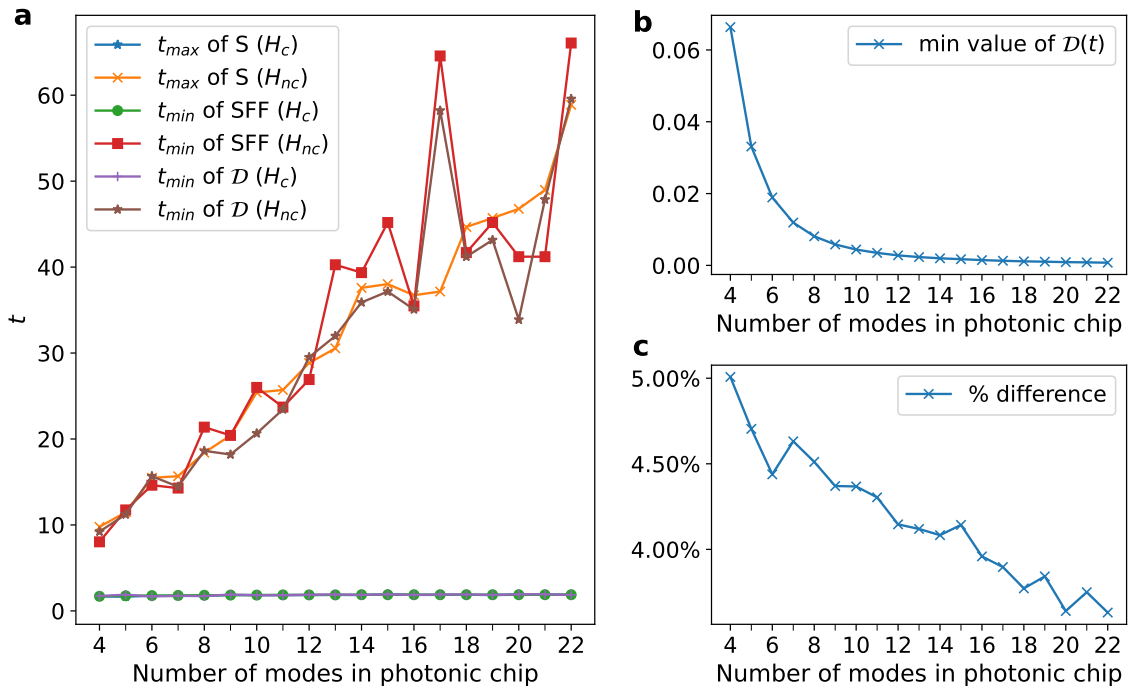


Fig. S4 Numerical results demonstrating that quantum chaos probes scale favourably as the system size is increased. **a**, For both the chaotic and non-chaotic cases, we plot the minimum-SFF time, maximum Shannon-entropy time, and also the time where the empirical distribution of probability values are the closest to the Porter–Thomas distribution, and the time at which the Participation Ratio (PR) of the OTOCs reaches its maximum value. For the chaotic times, all four times converge and are approximately constant, unlike in the non-chaotic case. **b**, We show for the chaotic case that as we scale the system size, the empirical distribution of probability values becomes closer to the Porter–Thomas distribution at t^* . **c**, We plot the percentage difference between Eq. 7 and the simulated maximal value of the Shannon Entropy, obtained by simulating Boson Sampling experiments with 2000 instances. We see that the maximal value of the Shannon Entropy gets closer to Eq. 7 as the system size increases.

E.5 Summary

Putting these observations together, we obtain the following picture for chaotic Hamiltonians. The spectral form factor exhibits a dip–ramp–plateau structure, with a minimum at $t \approx t^*$. Near this time, the unitary evolution e^{-iHt} approaches Haar-random behavior. Consequently, the boson sampling output probabilities become closest to the Porter–Thomas distribution, leading to a minimum in $\mathcal{D}(t)$. At the same time, the Shannon entropy is maximized and approaches its Haar-average value. For integrable systems, where the SFF does not exhibit such a structure, we do not expect corresponding features in $\mathcal{D}(t)$ or $S_{\text{avg}}(t)$.

Appendix F Numerical Evidence that Probes Scale Well with System Size

As can be seen in Fig. S4, the percentage difference between Eq. 8 and the value of $\max_t(S_{\text{avg}}(t))$ obtained by simulating Boson Sampling experiments for the chaotic case. We see that the finite size effects reduce as the number of modes increases, which is what we expect from Appendix E. We also see that the minimum point of \mathcal{D} gets closer to 0 as the number of modes increases, which is consistent with the reduction in finite size effects. Finally, we also see that when we simulate Boson Sampling experiments for an increasing number of modes, for the chaotic case, three times: minimum SFF time, maximum averaged Shannon entropy time and the minimum $\mathcal{D}(t)$ time are all the same regardless of the number of modes used, whereas in the integrable case, these three times are not the same, with the difference becoming larger at higher number of modes. Taken together, these observations suggest that the two probes of quantum chaos studied here become more effective as the system size increases.

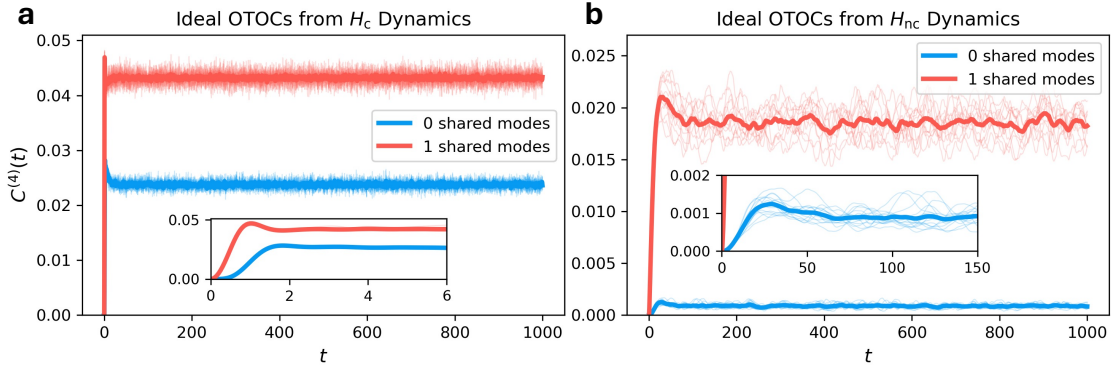


Fig. S5 **a,b**, Ideal 4-point OTOCs for H_c and H_{nc} respectively are shown for all collision-free output configurations, obtained from averaging over 2000 Hamiltonian instances. Blue (red) curves correspond to configurations with 0 (1) shared occupied modes with the input configuration. Thin curves denote individual configurations, while bold curves represent sector averages. Insets show short-time dynamics.

Appendix G OTOC Dynamics in Boson Sampling

As discussed in Section 4.3 and Ref. [40], the output probabilities in a boson sampling experiment can be mapped to four-point out-of-time-ordered correlators. This correspondence implies that the temporal behavior of the measured output probabilities reflects the scrambling properties of the underlying unitary dynamics. Figure S5 shows the ideal OTOCs for all collision-free output configurations under chaotic and integrable dynamics, grouped by their overlap with the input state. Generally, the OTOC dynamics can be characterized by an initial growth phase up to a scrambling time t^* , after which the correlator saturates and fluctuates around a steady-state value [52]. In this appendix, we analyze both the short-time and long-time regimes of these OTOC-equivalent quantities and show how they can be used as additional diagnostics of chaotic versus integrable dynamics.

G.1 Short-Time Behavior

At short times, the four-point OTOC $C_{i,j,r,s}^{(4)}(t)$ can be expanded perturbatively in time. For a two-photon input state $\hat{a}_i^\dagger \hat{a}_j^\dagger |0\rangle$ and output modes r and s , the OTOC-equivalent observable is

$$C_{i,j,r,s}^{(4)}(t) = \langle 0 | \hat{C}_{i,j,r,s}^\dagger(t) \hat{C}_{i,j,r,s}(t) | 0 \rangle, \quad (\text{S30})$$

where $\hat{C}_{i,j,r,s}(t) = [\hat{a}_i^\dagger(t) \hat{a}_j^\dagger(t), \hat{a}_r \hat{a}_s]$ and the Heisenberg-evolved creation operator is given by $\hat{a}_i^\dagger(t) = \sum_k U_{ik}(t) \hat{a}_k^\dagger$. Substituting the Heisenberg-evolved operators into the commutator gives

$$\hat{C}_{i,j,r,s}(t) = \sum_{k,l} U_{ik}(t) U_{jl}(t) [\hat{a}_k^\dagger \hat{a}_l^\dagger, \hat{a}_r \hat{a}_s]. \quad (\text{S31})$$

Using the bosonic commutation relations gives the usual two-photon bosonic interference term,

$$C_{i,j,r,s}^{(4)}(t) = |U_{ir}(t)U_{js}(t) + U_{is}(t)U_{jr}(t)|^2, \quad (\text{S32})$$

up to the normalization convention used for collision-free output probabilities. Thus, the short-time behavior of the OTOC is determined by the leading powers of the single-particle transition amplitudes $U_{ab}(t)$. Expanding $U(t) = e^{-iHt}$, we have $U_{ab} = \delta_{ab} - itH_{ab} + \mathcal{O}(t^2)$. Therefore, diagonal amplitudes are of order unity at short times, $U_{aa}(t) = 1 + \mathcal{O}(t)$, while off-diagonal transition amplitudes are of order t , $U_{ab}(t) = \mathcal{O}(t)$ with $a \neq b$.

The power law then follows from the number of off-diagonal transitions needed to connect the input configuration (i, j) to the output configuration (r, s) . If the final configuration shares one occupied mode with the input configuration, for example $r = i$ and $s \neq j$, then $U_{ir}(t)U_{js}(t) =$

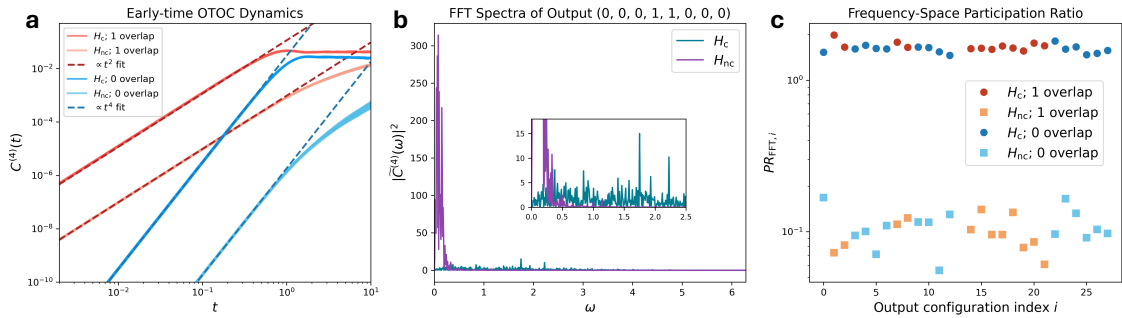


Fig. S6 **a**, Early-time OTOCs exhibit t^2 scaling for output configurations sharing one occupied mode with the input configuration and t^4 scaling for configurations with no shared occupied modes; dashed lines denote the fitted power-law scalings. All output configurations are plotted and grouped according to the number of shared occupied modes with the initial configuration. **b**, FFT power spectra $|\tilde{C}^{(4)}(\omega)|^2$ of the late-time OTOC fluctuations for the output configuration (0, 0, 0, 1, 1, 0, 0, 0) are shown for chaotic H_c (teal) and integrable H_{nc} (purple) dynamics. Before computing the FFT, the OTOCs from $t = 300$ to $t = 1000$ are normalized by their temporal mean values and shifted by subtracting unity. **c**, Frequency-space participation ratios PR_{FFT} of the Fourier-transformed OTOCs are shown for all output configurations except the initial configuration. Before computing the PR_{FFT} , the FFT power spectra in **b** are normalized such that the integrals are unity. Circular markers correspond to GOE dynamics, while square markers correspond to Poissonian dynamics.

$U_{ii}(t)U_{js}(t) = \mathcal{O}(1)\mathcal{O}(t) = \mathcal{O}(t)$, while the exchange term $U_{is}(t)U_{jr}(t)$ is at most of order t^2 . Hence, the leading contribution to the amplitude is of order t , and

$$C_{i,j,r,s}^{(4)}(t) \propto t^2, \quad (\text{S33})$$

for output configurations sharing one occupied mode with the input configuration. If there is no overlap between the input and output configurations, then all four single-particle amplitudes appearing in Eq. S30 are off-diagonal, $U_{ir}(t), U_{js}(t), U_{is}(t), U_{jr}(t) = \mathcal{O}(t)$. Both bosonic paths in Eq. S30 therefore contribute at order t^2 , so the probability scales as

$$C_{i,j,r,s}^{(4)}(t) \propto t^4. \quad (\text{S34})$$

More generally, the short-time scaling exponent is determined by the minimum number of off-diagonal transitions required to connect the input and output configurations. Configurations sharing occupied modes with the input state therefore dominate at early times, reflecting perturbative memory retention of the initial configuration.

This explains the two short-time power laws shown in Fig. S6a: configurations with one shared occupied mode scale as t^2 , while configurations with no shared occupied modes scale as t^4 . The scaling is determined by the perturbative structure of the single-particle transition amplitudes and therefore does not by itself distinguish chaotic from integrable dynamics. The difference between the two regimes appears only in the prefactors, with integrable (Poissonian) dynamics typically yielding smaller amplitudes, and in the long-time behavior shown below. Similar short-time power-law behavior has been observed in other systems, such as spin chains with random fields [52], confirming that this regime reflects general operator growth rather than chaos-specific features.

G.2 Long-Time Behavior and Fluctuations

At longer times, the OTOC approaches a steady-state value and exhibits fluctuations around it. The nature of these fluctuations provides additional information about the underlying dynamics. Fig. S6b shows the Fourier power spectrum of the time-dependent OTOC for a representative output configuration. In the chaotic case, the spectrum contains contributions from a broader range of frequencies, reflecting more complex temporal fluctuations and stronger mixing in Hilbert space. By contrast, the integrable spectrum is more localized, consistent with more regular and constrained dynamics.

G.3 Frequency-Space Delocalization

To quantify the spread of the OTOC in frequency space, we calculate the participation ratio of the Fourier-transformed correlator:

$$\text{PR}_{\text{FFT}} = \left[\int_0^\infty d\omega |\tilde{C}(\omega)|^4 \right]^{-1}, \quad \int_0^\infty d\omega |\tilde{C}(\omega)|^2 = 1, \quad (\text{S35})$$

where $\tilde{C}(\omega)$ is the normalized Fourier-transformed OTOC of a specific output configuration at late times. This quantity measures the effective number of frequency components contributing to the OTOC fluctuations: small values correspond to spectra concentrated around a few dominant frequencies, while large values indicate more delocalized spectra.

Fig. S6c shows that PR_{FFT} is systematically larger in the chaotic case than in the integrable case across all collision-free output configurations other than the initial state. This provides a quantitative measure of the enhanced complexity of temporal fluctuations in chaotic dynamics. Unlike the short-time scaling behavior, which is strongly organized by overlap sectors, the separation in PR_{FFT} persists broadly across output configurations, indicating that the long-time frequency-space complexity is governed more directly by the underlying dynamics. This long-time fluctuation behavior of the OTOC has also been observed in spin chains [52, 53].

G.4 Interpretation and Additional Remarks

Taken together, the results presented in this appendix provide a consistent picture of the OTOC dynamics in boson sampling. The short-time behavior is governed by the perturbative structure of the single-particle transition amplitudes and reflects general operator growth rather than chaos-specific behavior. In particular, the growth follows overlap-dependent power-law scaling, and configurations sharing more occupied modes with the input state dominate at early times.

At longer times, the OTOC temporal fluctuations and their frequency content can be used to provide qualitative and quantitative diagnostics of chaos. Chaotic dynamics exhibit broader frequency spectra and larger PR_{FFT} , consistent with enhanced scrambling and delocalization driven by chaotic evolution. These long-time fluctuations, therefore, provide a complementary probe of scrambling beyond the early-time growth regime.

These observations complement the diagnostics presented in Section 4 and provide additional tools for probing quantum chaos in boson sampling. While these frequency-space diagnostics provide useful additional insight, we emphasize that they should be interpreted qualitatively in the present finite-size system. A more systematic characterization of their scaling with system size would be an interesting direction for future work.